HHS Public Access

Author manuscript

Nature. Author manuscript; available in PMC 2024 June 15.

Published in final edited form as:

Nature. 2023 January ; 613(7943): 391–397. doi:10.1038/s41586-022-05566-4.

Structural basis of regulated m^{7}G tRNA modification by METTL1-WDR4

Jiazhi Li[1,2,3,*], **Longfei Wang**[2,4,5,*], **Quentin Hahn**[1], **Radosław P. Nowak**[2,3], **Thibault Viennet**[2,3], **Esteban Orellana**[1,2], **Shourya S. Roy Burman**[2,3], **Hong Yue**[2,3], **Moritz Hunkeler**[2,3], **Pietro Fontana**[2,4], **Hao Wu**[2,4], **Haribabu Arthanari**[2,3], **Eric Fischer**[2,3], **Richard I. Gregory**[1,2,6,7,8,9,10]

[1]Stem Cell Program, Division of Hematology/Oncology, Boston Children's Hospital, Boston, MA 02115, USA

[2]Department of Biological Chemistry and Molecular Pharmacology, Harvard Medical School, Boston MA 02115, USA

[3]Department of Cancer Biology, Dana-Farber Cancer Institute, Boston, MA 02115, USA

[4]Program in Cellular and Molecular Medicine, Boston Children's Hospital, Boston, MA 02115, USA

[5]School of Pharmaceutical Sciences, Wuhan University, Wuhan 430071, China

[6]Division of Hematology/Oncology, Boston Children's Hospital, Boston, MA 02115, USA

[7]Department of Pediatrics, Harvard Medical School, Boston, MA 02115, USA

[8]Harvard Stem Cell Institute, Cambridge, MA 02138, USA

[9]Harvard Initiative for RNA Medicine, Boston, MA 02115, USA

Summary

Chemical modifications of RNA have key roles in many biological processes[1–3]. N7-methylguanosine (m^{7}G) is required for integrity and stability of a large subset of transfer RNAs (tRNAs)[4–7]. METTL1-WDR4 complex is the methyltransferase (MTase) that modifies G46 in the variable loop of certain tRNAs and its dysregulation drives tumorigenesis in numerous cancer types[8–14]. *WDR4* mutations cause human developmental phenotypes including microcephaly[15–17].

[10]Corresponding author: Richard I. Gregory, rgregory@enders.tch.harvard.edu.
*These authors contributed equally

Author contributions

J.L. and R.I.G. conceived the project. J.L performed recombinant protein purification and ternary complex reconstitution. J.L., L.W and P.F. prepared and optimized samples for cryo-EM. L.W. performed cryo-EM data processing. J.L. built models with the assist from L.W., S.S.R.B. and M.H.. J.L., R.P.N. and E.S.F determined and refined the crystal structure of binary complex. J.L., Q.H., T.V. and H.Y. performed biochemical experiments. E.O., J.L. and Q.H. performed cellular experiments. R.I.G., E.S.F., H.A., and H.W. supervised the project. All authors organized and analyzed data. J.L., L.W. and R.I.G. wrote the manuscript with input from all authors.

Competing interests

R.I.G. is a co-founder and scientific advisory board member of 28/7 Therapeutics and Theonys. E.S.F. is a founder, science advisory board (SAB) member, and equity holder in Civetta Therapeutics, Lighthorse Therapeutics, Neomorph Inc (board of directors), and Proximity Therapeutics. SAB member and equity holder in Avilar Therapeutics and Photys Therapeutics. E.S.F. is a consultant to Novartis, Sanofi, EcoR1 capital, Avilar, and Deerfield. The Fischer lab receives or has received research funding from Astellas, Novartis, Voronoi, Interline, Ajax, and Deerfield. The rest of the authors declare no competing interests.

How METTL1-WDR4 modifies tRNA substrates and is regulated remains elusive[18]. Through structural, biochemical, and cellular studies of human METTL1-WDR4 we show that WDR4 serves as a scaffold for METTL1 and the tRNA T-arm. Upon tRNA binding, the αC region of METTL1 transforms into a helix, which together with the α6 helix secures both ends of the tRNA variable loop. Unexpectedly, we find that the predicted disordered N-terminal region of METTL1 is part of the catalytic pocket and essential for MTase activity. Furthermore, we reveal that Serine27 phosphorylation in the METTL1 N-terminal region inhibits MTase activity by locally disrupting the catalytic center. Our results provide a molecular understanding of tRNA substrate recognition and phosphorylation-mediated regulation of METTL1-WDR4, and reveal the presumed disordered N-terminal region of METTL1 as a nexus of MTase activity.

Keywords

epitranscriptome; tRNA; m^{7}G; METTL1; WDR4; methylation; structure; phosphorylation; cryo-EM; development; cancer

Introduction

Recent ‘epitranscriptome’ studies reveal critical roles of RNA modifications in various molecular, cellular, and developmental processes[1,2]. Several childhood developmental disorders are caused by mutations in genes encoding RNA-modifying enzymes, and dysregulation of certain RNA modifications is oncogenic[3,19,20]. tRNAs are the most highly modified class of RNAs that influences tRNA maturation, stability, and function[4,21,22]. Of these, N7-methylguanosine (m^{7}G) at position G46 in the variable loop is a prevalent modification in a large subset of tRNAs. m^{7}G46 interacts with C13-G22 in the D-loop to stabilize tRNA tertiary structure[5]. Impaired m^{7}G46 is associated with rapid tRNA decay (RTD) and altered expression[6,7]. m^{7}G46 is catalyzed by Methyltransferase 1 (METTL1) and its essential cofactor WD Repeat-Containing Protein 4 (WDR4)[8,9]. The METTL1-WDR4 complex is required for normal mRNA translation and mouse embryonic stem cell (ESC) proliferation and differentiation[23]. Mutations in *WDR4* are associated with developmental defects including primordial dwarfism, microcephaly, and Galloway-Mowat syndrome (GAMOS)[15–17]. Dysregulated METTL1-WDR4 drives tumorigenesis and this oncogenic function is linked to numerous different cancer types[10–14]. However, the lack of structural and mechanistic information on human METTL1-WDR4 remains a major obstacle to elucidating the m^{7}G46 modification process and development of MTase inhibitors as possible new anti-cancer drugs.

m^{7}G46 modification occurs in a large subset of tRNAs that contain the ‘RAGGU’ motif within the variable-loop[10,11,23]. *In vitro* MTase assays showed the importance of the D-arm and T-arm for m^{7}G modification by the yeast Trm8-Trm82 complex (orthologs of METTL1 and WDR4, respectively)[24]. A model for tRNA recognition was previously generated by computationally docking a tRNA structure into a structure of Trm8-Trm82[9]. The model implicated tRNA interaction with the positively charged surface of Trm8 without contact with Trm82 and is based on only a partial structure of the yeast complex that lacks regions

required for m^7G catalysis. It therefore remains unknown how the m^7G MTase complex specifically engages and modifies tRNA substrates.

Phosphorylation of METTL1 (Ser27) by protein kinase B (AKT) can inactivate MTase activity by an unknown mechanism[18]. Notably, Ser27 is located within the N-terminus of METTL1, for which no structural information is available and is predicted to be largely disordered[9]. Nevertheless, the flexible METTL1 N-terminus is conserved, implying essential functions.

Here, we report structures of the human METTL1-WDR4 heterodimer, and in complex with tRNA substrates, $tRNA^{Val}$TAC and $tRNA^{Phe}$GAA. The different tRNAs show a similar binding mode to METTL1-WDR4, in which the structural rearrangement of both the MTase complex and the tRNA are visualized. Combined with functional assays, we uncover the molecular mechanism for m^7G46 modification by METTL1-WDR4. We identify an essential role of the METTL1 N-terminus (residues 1-33) that while anticipated to be unstructured, plays a key role in formation of the MTase catalytic pocket. Strikingly, we furthermore uncover how S27 phosphorylation in the N-terminal domain of METTL1 inhibits MTase activity via a steric interference mechanism in the active site. Our findings uncover the molecular mechanism of tRNA substrate recognition by METTL1-WDR4, highlight the unanticipated role of the N-terminal region of METTL1 in tRNA modification, and explain the phospho-mediated regulation of MTase activity.

Results

Structures of METTL1-WDR4-tRNA

To visualize how human METTL1-WDR4 binds tRNA, we pursued cryo-EM studies of the METTL1-WDR4-$tRNA^{Phe}$ and METTL1-WDR4-$tRNA^{Val}$ complexes (Extended Data Fig. 1a–c). Monodisperse ternary complex samples were obtained using SEC and examined using native PAGE before cryo-EM screening and data collection (Extended Data Fig. 1d, e). Reconstructions of the METTL1-WDR4-$tRNA^{Phe}$ complex with S-adenosylhomocysteine (SAH) were refined to 3.3 Å (Fig. 1a, Extended Data Fig. 2a) and the METTL1-WDR4-$tRNA^{Val}$ complex to 3.6 Å (Extended Data Fig. 2b). Although both maps are anisotropic and to some extent challenging to accurately interpret in regions such as the distal part of WDR4 and tRNA (Extended Data Fig. 2c–h), model building in these regions was guided by a crystal structure obtained for the METTL1-WDR4 binary complex (Fig. 1b–d), AlphaFold 2 predictions, and published tRNA structures[25,26]. In both ternary complexes, the overall structures resemble a sail boat like arrangement with METTL1 and WDR4 as the stern and bow, respectively, and the tRNA as the sail that sits on top of METTL1-WDR4 and tilts sideways (Fig. 1b, c, Extended Data Fig. 3a–d).

METTL1, like other members of the Class I MTase family, shared the highly conserved Rossmann-like fold, comprising a seven-strand β-sheet flanked by six α-helices (Fig. 1b, Extended Data Fig. 4). WDR4 adopts a β-propeller structure with seven blades (B1-B7) (Extended Data Fig. 5a, b). The B2-B5 region of WDR4, which are in proximity to METTL1, are highly conserved (Extended Data Fig. 5c).

tRNA loading by METTL1-WDR4

To investigate whether tRNA binding causes structural rearrangements of METTL1-WDR4, we determined the crystal structure of the human METTL1-WDR4 binary complex to a resolution of 3.1 Å (Fig. 1d). In the crystal structure, the entire β-propeller of WDR4 and the following α-helix (residues 319-348) were modeled, but residues 26-33 from the N-terminal of METTL1 were not visible. Although the overall assembly of METTL1 and WDR4 was similar without tRNA, a superposition on WDR4 showed significant changes in METTL1 upon tRNA binding (Fig. 1e, Extended Data Fig. 6a). Four helices of METTL1 (α1, α2, α5, and α6) are shifted towards the tRNA. A loop (residues 164-173) connecting α1 and the core of the Rossmann fold of METTL1 forms a 3_{10} helix (hereafter referred to as αC helix), which is inserted into the groove of the tRNA elbow region. Interestingly, despite being highly conserved amongst eukaryotes (Extended Data Fig. 4), the residues 164-173 represent either a loop or are disordered in all known METTL1 structures (PDB: 3ckk, 7pl1, 2vdu and 2vdv). When superimposing the METTL1 structures in its tRNA-free and tRNA-bound states, the αC loop is the only region that undergoes structural rearrangement, suggesting that the αC helix of METTL1 facilitates tRNA recognition (Extended Data Fig. 6b and discussed later).

Interestingly, about 28% of the particles from the METTL1-WDR4-$tRNA^{Phe}$ dataset represent the binary complex and were used to reconstruct a cryo-EM map with a resolution of 3.5 Å (Extended Data Fig. 6c). Although the overall structure of the cryo-EM binary complex is similar to the crystal structure (Extended Data Fig. 6d), local resolution of the αC region was low and we were unable to model αC region confidently (Extended Data Fig. 6e, f).

The non-catalytic subunit WDR4 is required for MTase activity[8]. To explore the mechanistic basis for this requirement, we further analyzed the interface between METTL1 and WDR4 in the binary structure, and found that B4 of WDR4 contributes most interactions between the two proteins (Extended Data Fig. 7a). Salt bridges (between METTL1 K143 and WDR4 D166, METTL1 D261 and WDR4 H178), and hydrogen bonds (METTL1 Y37 and WDR4 E167, METTL1 N147 and WDR4 K168, and METTL1 K40 with the backbone of WDR4 L185) form the interface between METTL1 and WDR4. METTL1 K143, WDR4 D166, and WDR4 E167 are conserved among different species (Extended Data Fig. 4, 5b). Single alanine substitutions of some of these conserved residues abolished MTase activity (Extended Data Fig. 7b). In METTL1 or WDR4 KO cell lines (R1/E mESCs), the METTL1 K143A, WDR4 D166A, and WDR4 E167A variants could not rescue m^7G tRNA modification (Extended Data Fig. 7c, d). Thus, the interactions between METTL1 and B4 of WDR4 are necessary for MTase activity.

WDR4 acts as a scaffold for tRNA binding

We found B4 of WDR4 not only mediates the interaction with METTL1 but is also, together with B3, involved in tRNA binding (Fig. 2a, b). Positively charged residues are located on the top of B3 and B4, and are prone to form salt bridges with the phosphates of the T-arm of tRNA. Alanine substitutions of these residues showed varying effects with little effect on

MTase activity of R103A, R104A, and K122A, reduced activity with K83A, and no activity was observed for R165A or the R103/R104A double mutant (Fig. 2c).

Mutation of R170, located in B4 of WDR4, is a mutation linked to primordial dwarfism accompanied by distinct facial dysmorphism, brain malformation, and severe encephalopathy with seizures[15,17]. The presumed corresponding residue (K223) in yeast Trm82 (WDR4), forms a salt bridge with E204 of Trm8 (METTL1) (Extended Data Fig. 7e). Based on the Trm8-Trm82 structure, it was proposed that R170 variants disrupt the interaction of WDR4 with METTL1[15]. Interestingly, we find that in human, the R170 of human WDR4 likely does not interact with METTL1 but rather mediates intramolecular WDR4 interactions (Fig. 2b, Extended Data Fig. 7e, f). These comparisons were performed using the crystal structure of the METTL1-WDR4 binary complex since the relevant region is better resolved. The sidechain of R170 forms hydrogen bonds with the mainchain of G143 and P177, which are located in B3 and B4, respectively. Right alongside R170, the H144 of WDR4 B3 interacts with D164 and T162 of B4. Based on TCGA data, the H144P mutation occurs in lung cancer yet the mechanism and effect on the activity of the MTase complex is unknown. *In vitro* MTase assay showed R170Q and H144P variants totally abolished the MTase activity of METTL1, and the R170L decreased activity by a third (Fig. 2d). Therefore, these patient-derived mutation sites are involved in B3-B4 stabilization and are crucial for MTase activity.

To further verify the role of WDR4, we also tested the effects of individual amino acid substitutions of WDR4 in cells (Fig. 2e, Extended Data Fig. 7g). The m^7G level was almost undetectable in rescue experiments using WDR4 R170L, R170Q, and H144P WDR4 variants in WDR4 KO cells. Similarly, charge reversal (mutated to E) of R165 and R103/R104 was also incapable of rescuing the m^7G levels when introduced into WDR4-deficient cells. Altogether, we identify that WDR4 acts as a scaffold to interact with METTL1 and support tRNA binding. Importantly, mutations that impair the rigidity of the scaffold decrease MTase activity.

tRNA bending by METTL1-WDR4

The tRNA G46 is buried in the variable loop (Fig. 1b, Extended Data Fig. 1a), and needs to be flipped into the catalytic site for modification by METTL1, which could be induced by tRNA bending[9,27]. Three dimensional (3D) variability analysis performed with cryoSPARC[28] suggested that the $tRNA^{Phe}$ underwent bending (Video 1), and we therefore clustered particles based on the principal components in the 3D variability analysis and selected two distinct clusters from METTL1-WDR4-$tRNA^{Phe}$ for reconstructions (Extended Data Fig. 2a). Superposition of models that were rigid body fit to the maps of the two states (named state A, pre-bending; state B, bending) showed that while the position of most of the $tRNA^{Phe}$ remained unchanged relative to the MTase, the anticodon-arm was bent towards METTL1 and accompanied with local unwinding of the variable loop (Fig. 2f, Extended Data Fig. 2h). METTL1 is closer to the tRNA in state B than in state A. As a result, the variable loop is positioned closer to the catalytic pocket of METTL1 and is partially unwound, which likely facilitates base flipping of tRNA G46.

METTL1 recognizes tRNA via two helices

Due to the induced fit, sidechain densities for the METTL1 αC and α6 helices are absent from the experimental density but the mainchain atoms can be traced with high confidence (Extended Data Fig. 2g). These two helices contain multiple conserved and positively charged residues (Fig. 2g, h, Extended Data Fig. 4). METTL1 H165, K167, R168, and K170 of αC are close to the T-arm and variable-loop junction (T-V joint), and the K243 and R246 of α6 helix are close to the Anticodon-arm and Variable-loop junction (A-V joint). MTase activity was decreased by alanine-substituted mutations of H165, K170, and K167 in αC (Fig. 2i). Single mutation of METTL1 K243 and R246 in α6 slightly decreased MTase activity but the double mutation decreased the activity by half. *In vivo*, the METTL1 αC and α6 variants (K243A/R246A, H165, K167A, and K170A) were unable to rescue the m^7G level (Fig. 2j, Extended Data Fig. 7h). These results support a model in which METTL1 binds to the tRNA variable loop through two helices but requires WDR4 as a 'scaffold' (Fig. 2k). B4 of WDR4 serves as an important bridge between WDR4 and METTL1.

Role of N-terminus in METTL1 activity

The N-terminal region (residues 1-33) of METTL1 is predicted to be disordered, consistent with the lack of electron density in crystal structures of the human METTL1 (PDB: 3ckk, 7ogj), the yeast ortholog (PDB: 2vdc, 2vdu), and our crystal structure of the METTL1-WDR4 binary complex (Extended Data Fig. 8a). However, the high degree of amino acid sequence conservation (residues 16-50) and the presence of a regulatory phosphorylation site (S27) that inhibits METTL1 activity[18] point towards an important role of the N-terminus (Extended Data Fig. 4). We therefore analyzed the AlphaFold[25] predicted structure of a METTL1-WDR4 dimer (Fig. 3a, Extended Data Fig. 8b), which consistent with our structures has residues 34-54 attached to the surface of METTL1 and extending towards the catalytic pocket (Fig. 1b, d, 3a, b). Residues 16-33 (AlphaFold) thread through the catalytic pocket of METTL1, with residues 28-32 turning and entering the catalytic pocket where H26 and S27 are buried. In our ternary cryo-EM structures, the weak density for residues 26-33 can be traced and agrees well with the predictions from AlphaFold (Fig. 3a, b, Extended Data Fig. 2g) indicating that the 26-27 segment contributes to the catalytic pocket. Interestingly, residues 21-25 were predicted to exit and contact one end of METTL1 α2 helix, which might act as an anchor for residues 16-20 (Extended Data Fig. 8c). When superposing the predicted METTL1 structure onto the ternary complex structure, the 16-20 segment is positioned between the α2 helix and tRNA, which potentially interacts with tRNA (Extended Data Fig. 8d).

To investigate whether the N-terminus binds to the METTL1 core, we utilized Nuclear Magnetic Resonance (NMR). We expressed isotope-labeled 1-75 segment of METTL1 and confirmed that it is largely disordered, except for the 45-55 segment that exhibits secondary structure (Extended Data Fig. 8e). We then used NMR titration experiments to map the interaction of the METTL1 core onto its N-terminus. Notably, we observed two interacting segments: residues 35-55 that interact with higher affinity (this corresponds to the segment seen in our binary complex structure and the element possessing secondary structure) and residues 18-27 that interact with an apparent lower affinity (Fig. 3c, **WT, black**). These results confirm that residues 18-27 associate with the METTL1 core.

To probe the functional importance of the N-terminus, we performed truncation and mutagenesis studies on the N-terminus and α2 helix of METTL1 *in vitro*. Truncation studies show that deletion of residues 1-15 of METTL1 has little effect on MTase activity, but deletion of residues 1-20 or more leads to an inactive enzyme (Fig. 3d). The single alanine substitution of K18 of METTL1 significantly decreased MTase activity. In the TR-FRET competitive binding assay, the binding affinity of METTL1(Δ1-20aa)-WDR4 and METTL1(Δ1-36aa)-WDR4 truncations to tRNA was slightly lower than the full-length METTL1-WDR4 (Extended Data Fig. 8f). These results are consistent with our proposed role of residues 16-20 in MTase activiy and possible contact with the anticodon branch of tRNA. Single alanine substitution of K111 and D118 (α2) showed moderate effect on the methylation activity of METTL1, but R109A (α2) totally abolished the activity (Fig. 3e). Furthermore, NMR experiments showed that R109A/K111A mutation in the α2 helix decreased its association with residues 24-27 in the N-terminal region of METTL1 (Fig. 3c, **R109A/K111A, red**). We also validated these results with *in vivo* experiments (Fig. 3f, Extended Data Fig. 8g). The METTL1 R109A and K18A (N-terminus) mutants were unable rescue the m^7G level in METTL1 KO mESC cell lines, while K111A could partially rescue m^7G tRNA modification. The METTL1(Δ1-15aa) completely restored m^7G, whereas the METTL1(Δ1-20aa) did not rescue. Therefore, the residues16-27, as a highly conserved part of the METTL1 catalytic pocket, are essential for METTL1 activity.

Phosphorylation regulation of METTL1

Human METTL1 is inactivated by protein kinase B (AKT)-mediated S27 phosphorylation[18]. This phosphorylation site is located at the bottom of the U-shaped N-terminus, which is buried in the catalytic pocket (Fig. 3a, b). *In vivo*, overexpression of S27D (mimic S27 phosphorylation) METTL1 could not rescue m^7G levels (Extended Data Fig. 8h). In the METTL1-WDR4-$tRNA^{Phe}$ structure, SAH was stabilized in the conserved SAM binding pocket. The sulfur atom of SAH, where the methyl-group should be in a SAM molecule, points into the catalytic pocket. A cluster of charged residues D163, E240, and R109 are presented in the METTL1 catalytic pocket that are likely involved in the catalytic process (Fig. 3g, Extended Data Fig. 8i). Interestingly, S27 is in proximity to this cluster but does not directly interact with any of these residues. To understand the molecular mechanism by which S27 phosphorylation in the N-terminal region of METTL1 controls its catalytic activity, we made a series of amino acid substitutions to identify the determinants (charge and size) of METTL1 inactivation by phospho-serine 27 (Fig. 3h). Removing the hydroxyl group from the serine (S27A) showed comparable activity with the wild type. Sidechains with similar lengths (S mutated to C or I) were tolerated, while negatively charged and phospho-mimetic (S27D), longer, and positively charged (S27K), and bulky aromatic (S27W) side chains, all inactivated METTL1. In our current model, METTL1 H26-S27 are in close proximity to the sidechain of R109 on the α2 helix (Fig. 3i). Modelling shows that the phosphate group of phosphorylated S27 would clash with either the side chain of R109 (Fig. 3j) or backbone of A21 on the D-arm of the tRNA (depending on the sidechain conformation). Therefore, we hypothesized that S27 phosphorylation induces steric hindrance which results in the destabilization of the network of interactions between the N-terminus, active site, and α2 helix. We tested this hypothesis by performing NMR assays with S27D mutant of the N-terminus, and indeed observed a specifically reduced

interaction with residues 24-27 of METTL1 (Fig. 3k). The steric effect and possible rotamer conformations of phosphorylated S27 might place its phosphate group closer to the D-arm of tRNA (Fig. 3j). The introduction of the negative charge by phosphorylation might repel the tRNA and cause further local shifting of the N-terminal residues, to disrupt the catalytic center and inhibit MTase activity dramatically.

To get molecular insight into the methylation mechanism of METTL1-WDR4, we modeled G46 alone in the catalytic pocket of METTL1 to allow for an SN_2-type nucleophilic reaction (Extended Data Fig. 8j). The N7 atom of G46 (attacking nucleophile) is co-linear with the S-CH_3 group of SAM (donor). Charged residues D163 and R109 potentially orient the target guanine proximal to the donor whereas residues E240 and H26 can potentially interact with the G46 or neighboring bases to facilitate the methyl transfer. Interestingly, *in vitro* assays showed the MTase activity is not sensitive to lower pH buffer (pH< 6.0) but is completely abolished by the H26A mutant. This suggests that H26 does not promote reaction chemistry as a proton shuttle in catalysis but is instead involved in the reaction process possibly by stabilizing a neighboring base with its aromatic ring (Extended Data Fig. 8k, l). Taken together, these findings are highly consistent with a steric hindrance model to explain phosphorylation-mediated regulation of METTL1 activity, whereby phosphorylated S27 locally disrupts the catalytic center including METTL1 N-terminal residues 24-27 to prevent G46 methylation.

Discussion

We present structures of the human METTL1-WDR4 heterodimer, and in complex with tRNAs to provide molecular insights into substrate recognition, modification, and catalytic regulation by the m^7G MTase complex. METTL1 and WDR4 form a heterodimer to provide a binding surface for their substrates. We reveal that METTL1 is the primary platform for tRNA binding, and WDR4 serves as a supporting scaffold. The tRNA loading process involves the reconfiguration of METTL1 (Fig. 4a, b). Furthermore, we provide evidence that two α-helices cooperate with the METTL1 N-terminal region to recognize and facilitate bending of the tRNA for methylation (Fig. 4c). Lastly, we identify the METTL1 N-terminus as an essential feature of the catalytic pocket, and present a steric hinderance and charge-mediated model to explain regulation of MTase activity by METTL1 S27 phosphorylation (Fig. 4a, d).

A growing list of recent studies highlight the importance of METTL1-WDR4 oncogenic activity in many different cancer types, suggesting that inhibition of this MTase complex represents a promising new cancer therapeutic strategy. The mechanistic insights presented here will facilitate the design and development of anti-cancer drugs targeting METTL1-WDR4.

Methods

Cloning, protein expression and purification

The codon optimized (*E. coli* expression) full-length human *METTL1* and *WDR4* genes were synthesized from GENEWIZ and subcloned into **pETDuet-1** vector containing a

His_6 tag at N-terminal of WDR4. Mutated and truncated constructions were generated using Q5 site-directed mutagenesis kit (E0554S, NEB) or HiFi DNA assembly master mix (E2621S, NEB). The METTL1 and WDR4 proteins were co-expressed in *E. coli* Rosetta (DE3) (Sigma) cells that were induced with 0.5 mM isopropyl-1-thio-b-D-galactopyranoside (IPTG) at OD_{600} = 0.6 at 16 °C overnight. Cells were harvested and sonicated in buffer containing 50 mM Tris-HCl, pH 8.0, 200 mM NaCl, 5% glycerol, 5 mM mercaptoethanol (β-ME) and 1 mM PMSF. The lysate was cleared by centrifugation and incubated with Ni Sepharose (QIAGEN). The bound protein was eluted with buffer containing 200 mM imidazole and was further purified by combined Q column and Heparin column (GE healthcare), and polished by size-exclusion chromatography (Superdex 200 Increase 10/300, GE Healthcare) in a buffer containing 50 mM Tris-HCl, pH 8.0, 150 mM NaCl and 1mM Tris(2-carboxyethyl)phosphine hydrochloride (TCEP). Finally, METTL1-WDR4 complex was concentrated to about 10 mg/ml for EM and crystallization use.

In Vitro Methylation Assay

The tRNA probe (Human_tRNA^{Val}TAC) was synthesized (Horizon) as the sequence of 5'-GGUUCCAUAGUGUAGCGGUUAUCACGUCUGCUUUACACGCAGAAGgUCCUGGGUUCGAGCCCCAGUGGAACCA-3' (Extended Data Fig.1b). The RNA probe was annealed at 95°C for 5min before reactions. METTL1-WDR4 complex (wild type or variants) were purified by Ni affinity chromatography. Optimized concentration of tRNA probe (100 nM) and METTL1-WDR4 (10 nM, wild type or variants) were applied to the reactions and followed the same protocol of previous study[10]. In the MTase assay testing the effects of buffer pH, the Tris buffer (pH 7.4) was substituted with sodium phosphate buffer (pH 5.6, 5.8, 6.0 and 7.4). Scintillation signals were measured using the Tri-Carb 2910 TR instrument (Perkin Elmer).

Size exclusion co-migration assay

METTL1-WDR4 complex were incubated with the tRNA^{Phe} (R4018, Sigma) and SAH, or with tRNA^{Val} (synthetic RNA, Horizon) and SAM at room temperature for 1h, respectively. The molar ratio of protein, tRNA and compound is 1:1.4:1.5. Incubated ternary complex samples, METTL1-WDR4 binary complex and tRNA were applied to a Superdex 200 Increase 10/300 (GE Healthcare) separately. Peak fractions were analyzed by native PAGE and stained with EB and G250 to visualize the tRNA and protein complex, respectively.

TR-FRET assay

The purified full-length METTL1-WDR4 complex were labeled with BODIPY (D2184, ThermoFisher) as described previously[29]. tRNA^{Val} was labeled with biotin by 5' EndTag™ DNA/RNA Labeling Kit (MB-9001, VECTOR) according to the vendor's procedures.

In the competitive assay, dilution of unlabeled apo METTL1, full-length or truncated METTL1-WDR4 complex were added to assay mix with final concentrations of 2 nM Tb-strep, 10 nM tRNA-Biotin, 40.5nM BODIPY-METTL1-WDR4, 121.5nM SAM and 100 nM non-specific RNA in a buffer containing 50 mM Tris-HCl, pH 8.0, 150 mM NaCl and 1mM TCEP. TR-FRET assays were performed in 384-well microplates (Corning, 4514) with 15 μL final assay volume. Before TR-FRET measurements were conducted, the reactions

were incubated for 15min. After excitation of terbium fluorescence at 337 nm, emission at 490 nm (Terbium) and 520 nm (BODIPY) were recorded with a 70 μs delay over 130 μs to reduce background fluorescence and the reaction was followed over >20 or >100 second cycles of each data point using a PHERAstar microplate reader (BMG Labtech Model FS). The TR-FRET signal of each data point was extracted by calculating the 520/490 nm ratio. Statistical calculations were performed using Prism 8.0.2.

Crystallization, Data Collection and Structure Determination

The recombinant METTL1-WDR4 complex was incubated with three-fold molar excess of SAM and further purified by Superdex 200 Increase 10/300 column (GE Healthcare). The sample was concentrated to 10 mg/ml for crystallization. Crystals of METTL1-WDR4 complex were obtained by mixing 75 nL complex solution and 75 nL of reservoir solution using an NT8 (Formulatrix), and were grown by the sitting drop vapor diffusion method at 20 °C. Crystals of METTL1-WDR4 complex were grown from 2 M $(NH_4)_2SO4$, 0.2M K Na Tartrate, 0.1 M Na_3 Citrate pH 6.5 for three weeks. All crystals were cryo-protected using corresponding reservoir buffers supplemented with 20% ethylene glycol and flash frozen in liquid nitrogen. All diffraction data sets were collected at the APS Chicago on beamlines 24-ID-C and 24ID-E at 100K. Data were indexed and integrated using RAPS pipeline from APS Chicago[30]. A 3.1 Å resolution dataset was collected at a wavelength of 0.97918 Å. The phases of METTL1-WDR4 structure was solved by molecular replacement using the program Phenix[31]. The METTL1 (PDB code 3ckk) and WDR4 (originating from chain D of Trm8-Trm82 complex, PDB code 2vdu) were used as separate search models. The model was adjusted using Coot and structure refinement was performed using in Phenix and autoBUSTER (version 2.10.4). The Ramachandran plot shows that 93.89% of residues are in favored regions, with the remaining in allowed regions. In the final coordinate file of 7U20, residues 34-56 and 75-265 of METTL1, and residues 0-44 (residue 0 is from protein tag) and 60-348 of WDR4 are modeled. All statistics of data processing and structure refinement of METTL1-WDR4 complex are summarized in Extended Data Table 1. The structure figures were prepared using PyMOL, and model quality was assessed with MOLPROBITY(version 4.2)[32]. Structural biology applications used in this project were compiled and configured by SBGrid[33].

EM sample preparation and data collection

The METTL1-WDR4-$tRNA^{Phe}$ complex was reconstituted by incubating METTL1-WDR4, $tRNA^{Phe}$ (R4018, Sigma) and SAH at the molar ratio of 1:1.2:1.5 at room temperature for 1h. The ternary complex was further purified on a Superdex 200 Increase 10/300 column (GE Healthcare) in buffer containing 50 mM Tris-HCl, pH 8.0, 150 mM NaCl and 1mM TCEP. Samples used for electron microscopy were measured for final absorbance of 0.2-1.0 using a Nanodrop spectrophotometer. The METTL1-WDR4-$tRNA^{Val}$ complex was reconstituted by incubating METTL1-WDR4, annealed $tRNA^{Val}$ (synthetic RNA, Horizon) and SAM, in the same conditions as above. Both samples were checked for morphology and homogeneity using negative-staining electron microscopy. For each ternary complex, 2.5 μl sample (A280=0.05) was placed on a glow-discharged carbon film copper grid (CF-400CU, Electron Microscopy Sciences). After a 60 seconds incubation, the grid was stained in 2%

uranyl formate for 30 seconds, air dried, and imaged on a Tecnai G2 Spirit BioTWIN microscope at Harvard Medical School Electron Microscopy Facility.

A 3 μl drop of the METTL1-WDR4-tRNA complex was applied to glow-discharged Quantifoil R1.2/1.3 400 mesh copper grids (Electron Microscopy Sciences). The grids were blotted for 4 s in 100% humidity at 4 °C, and plunge-frozen using the FEI Vitrobot Mark IV. Cryo-EM data collection of METTL1-WDR4-tRNA^{Phe} complex was performed on a 300 keV Titan Krios microscope (FEI) with a K3 direct electron detector (Gatan) using Latitude-S (Gatan Microscopy Suites software package MODEL 700.LS.731) at the National Cancer Institute's National Cryo-EM Facility. For the initial dataset, 5990 movies were collected in counting mode, with 40 frames per movie, 3.6 s exposure time, 60 $e^{-}/Å^2$ accumulated dose, and 1.08 Å pixel size. For the final dataset, 10,415 movies were collected in counting mode, with 40 frames per movie, 3.4 s exposure time, 50 $e^{-}/Å^2$ accumulated dose, and 1.08 Å pixel size.

Cryo-EM data collection of METTL1-WDR4-tRNA^{Val} complex was performed on a 300 keV Titan Krios microscope (FEI) with a K3 direct electron detector (Gatan) using SerialEM (version 3.8.5) at the Harvard Center for Cryo-Electron Microscopy (HC2EM). 5095 movies were collected in counting mode, with 50 frames per movie, 1.5 s exposure time, 51.8 $e^{-}/Å^2$ accumulated dose, and 0.825 Å pixel size.

Cryo-EM data processing and model building

For METTL1-WDR4-tRNA^{Phe} initial dataset, movies were motion-corrected using MotionCor2[34]. Patch contrast transfer function (CTF) estimation was performed using cryoSPARC[28]. Particles were initially picked using blob picker in cryoSPARC and subjected to 2D classification. Selected classes representing the ternary complex only accounted for ~3% of the total particles, and are used for ab-initio 3D reconstruction to generate a reference model. For METTL1-WDR4-tRNA^{Phe} final dataset, 10,415 movies were collected. Motion correction and CTF estimation were performed in the same way as in initial dataset. Supervised particle picking was carried out using the trained model from dataset I in Topaz[35]. After 2D classification, 634,274 particles were selected for ab-initio 3D reconstruction followed by 3D classification (heterogeneous refinement). 28% of the particles were binary complex without the tRNA and were used to reconstruct a 3.5 Å cryo-EM map. Two 3D classes of METTL1-WDR4-tRNA^{Phe} ternary complex (51% of the particles) were selected for another round of 2D classification to remove bad particles. After Bayesian polishing (Relion)[36] and non-uniform 3D refinement (cryoSPARC)[37], the map resolution of METTL1-WDR4-tRNA^{Phe} ternary complex reached 3.3 Å. For METTL1-WDR4-tRNA^{Val}, 5,094 movies were collected. The image processing procedures were the same as for METTL1-WDR4-tRNA^{Phe} dataset, with the exception that no binary complex class was found after 3D classification. 31% of the particles were selected for Bayesian polishing and non-uniform 3D refinement, yielded a map with a resolution of 3.6 Å. 3D variability analysis of METTL1-WDR4-tRNA^{Phe} were carried out in cryoSPARC[38] based on the non-uniform refinement with the low-pass filter set at 5 Å and number of modes set to 3 (Extended Data Fig. 2a). Each of the three components from 3D variability analysis represent a certain motion that contribute to the data variability. A video of the component

1 that represents the tRNA melting was generated (Video 1). Particles were clustered into 4 groups based on the principle components and all 4 groups were subjected to 3D refinement (Extended Data Fig. 2a). The cryo-EM map of METTL1-WDR4-tRNA^{Phe} is auto-sharpened by NU-refinement in CryoSPARC with a B-factor of −125.3. The sharpening B-factor for the cryo-EM map of METTL1-WDR4-tRNA^{Val} is −147.8. In both METTL1-WDR4-tRNA^{Phe} and METTL1-WDR4-tRNA^{Val} maps, we observed some degree of variations in local and directional resolutions, which could be explained by flexibility and preferred orientations[39] (Extended Data Fig. 2c–h). Consequently, ambiguous densities are present in a few regions of the sharpened maps. To overcome these limitations, DeepEMhancer were used to post-process the cryo-EM maps of METTL1-WDR4-tRNA^{Phe} and METTL1-WDR4-tRNA^{Val} to facilitate model building[40]. The initial model of METTL1-WDR4 was generated by rigid body fitting of the METTL1-WDR4 crystal structure model into the cryo-EM maps using ChimeraX[41]. The N-terminal region (residues 26-33) of METTL1 are modeled based on AlphaFold prediction in agreement with weak density and refined restrained to the conformation of the prediction. The tRNA^{Phe} was modeled using a yeast tRNA^{Phe} (PDB: 1EHZ). The tRNA^{Val} was homology modeled using a rabbit tRNA^{Val} (PDB: 3JAG, chain 2). Inspection, model building, and manual adjustments were carried out in Coot[42]. Real-space refinements were performed using Phenix[31]. The crystal structures and AlphaFold predict METTL1 N-terminal region (residues 1-33) were used as reference model restraints in Phenix refinements. For the final coordinate file of 8CTH (METTL1-WDR4-tRNA^{Phe}), residues 26-54 and 76-262 of METTL1, residues 6-28, 36-43, 62-233 and 244-318 of WDR4, nucleotides 1-74 of tRNA (Phe) and cofactor SAH are modeled. For the final coordinate file of 8CTI (METTL1-WDR4-tRNA^{Val}), residues 34-54, 77-125 and 131-262 of METTL1, residues 13-28, 62-233 and 244-318 of WDR4, and nucleotides 1-16 and 18-71 of tRNA (Val) are modeled. All statistics of data processing and structure refinement of cryo-EM structures are summarized in Extended Data Table 2. All representations of densities and structural models were generated using Chimera, ChimeraX and PyMOL Molecular Graphics System, Version 2.0 Schrödinger, LLC.

Rescue experiments

Mouse METTL1 KO R1/E ESCs from previous study[23] were used for METTL1 rescue experiments. In the case of WDR4 rescue experiments, new WDR4 KO were generated from mouse R1/E ESCs (gift from Dr. Lizi Wu, ATCC, SCRC-1036) following our previous protocol[23]. KO cell lines were cultured in Serum/LIF medium [DMEM (Gibco) with 1000u/ml mLIF (Gemini), 15% stem cell FBS (Gemini),1X Sodium Pyruvate (Gibco), 1X NEAA (Gibco), 1X L- glutamine (Gibco), 50μM 2-mercaptoethanol (ThermoFisher) and 1% Penicillin-Streptomycin (Gibco)] in a 5% CO_2 cell culture incubator at 37°C. Cells were cultured in feeder free condition in gelatin coated dishes (0.1% gelatin solution for 30 minutes at 37°C) to enhance cell attachment. For rescue experiments, cells were first washed with PBS twice and then trypsinized (0.1% trypsin in PBS) at 37°C for 3 minutes. Cells were then resuspended in Serum/LIF medium and counted. Then the METTL1, WDR4 or empty vector plasmids (10μg) were transfected into mESCs (~4 x10^6 cells) using the reverse transfection method with Lipofectamine 2000 (Invitrogen, 20 μL). Cell media was replaced daily and cells were collected 48 hours post transfection and split into two for RNA and protein isolation respectively.

Northwestern Blot and Western Blot

For Northwestern blot, 10 μg total RNA samples were mixed with 2X TBE loading buffer (Bio-Rad) and incubated at 95°C for 5 min. The samples were then loaded into 15% TBE-UREA (Bio-Rad) gels to separate the RNAs by molecular weight. Next, the RNAs were transferred onto a positive charged nylon membrane and crosslinked with UV. Next, membranes were immunoblotted with mouse monoclonal anti 7-methylguanosine (m^7G) (Clone 4141-13, MBL International, RN017M, 1:1000) and detected using the ECL method. For loading control the membrane was then blotted with radioactive labeled probes against U6 snRNA. Botted membranes were exposed to autoradiography films. For western blotting, cell pellets were resuspended in passive lysis buffer (Promega), supplemented protease inhibitors (cOmplete, Roche). Protein concentrations were assessed by Bradford assay (5000006, Bio-Rad) and an equal amount of protein was loaded per lane. Prior to loading, the samples were supplemented with SDS-PAGE sample buffer and β-mercaptoethanol was added to each sample. 10-40 μg of protein was separated on SDS-PAGE gels (4-20%), and blotted onto nitrocelullose membranes (Thermofisher). Membranes were then immunoblotted with the following antibodies: β -Actin (Abcam, ab8229, 1: 10000), METTL1 (Proteintech, 14994-1, 1: 2000), and WDR4 (Clone EPR11052, Abcam, ab169526, 1: 2000). Membranes were imaged using the Odyssey Imaging System, Image Studio (Li-Cor, Version 5.2.5).

AlphaFold prediction

Full length sequences of human METTL1 and WDR4 were input to AlphaFold 2.2 with Amber refinement[25]. To assess the position of WDR4 relative to METTL1, AlphaFold was run in the *ptm* mode, and the expected position error between the two proteins was extracted. An expected error of <5 Å was used as the criterion to determine interaction. Low confidence regions (plDDT < 70) including the glycine linker were removed to obtain the final model.

NMR spectroscopy

NMR experiments were conducted on Avance III Bruker (version 3.4) spectrometers operating at 600 and 800 MHz, equipped with three-channel ^{1}H, ^{13}C, ^{15}N cryogenically cooled probes. If not stated otherwise, experimental temperature was set to 15 °C. Data were processed using NmrPipe[43] and analyzed using CCPNmr Analysis[44]. A sample of 420 mM $^{15}N^{13}C$-labeled METTL1 1-75 was prepared in 50 mM NaPi pH=6.0, 100 NaCl, 1mM TCEP and 5 % v/v $^{2}H_2O$ for backbone assignments. The assignment routine employed regular HSQC, HNCA, HN(CO)CA, HNCO, HN(CA)CO, HN(CA)CB and CBCA(CO)NH experiments. All 3D experiments were set up with 10% non-uniform sampling using Poisson-Gap sampling[45] and reconstructed using the hmsIST protocol[46]. 91% of non-proline residues were assigned. Chemical shift assignments have been deposited in the BMRB under accession number 51362. Secondary structure predictions were obtained from the Talos-N algorithm[47] and proved that most of the construct is disordered, except for the 46-55 segment which exhibits 40-70% secondary structure (in line with the presence of a short beta-strand in some crystal structures). Assignments were readily transferred to the S27D mutant. Given the impossibility to express a truncated construct of METTL1 for direct

interaction studies, we utilized a competition assay in which ^{15}N-labeled METTL1 1-75 competes off the N-terminus of unlabeled METTL1. Samples of 23, 46 and 92 mM 1-75 were measured with and without 230 mM of unlabeled FL-METTL1, corresponding to 0, 2.5, 5 and 10 molar equivalents. SOFAST-HMQC experiment with a recycle delay of 0.2 s were used for accelerated sampling. Titration experiments showed line broadening of a subset of peaks, which indicates a slow exchange binding mode on the NMR timescale. Due to the nature of the assay and the use of SOFAST, measurement of peak intensities is not quantitative, however this allows mapping of the interaction onto the 1-75 fragment. To validate our NMR results in physiological conditions, we reproduced our competition assay at pH=7.4 and both 15 and 25 °C. 8 peaks disappeared from the spectrum due to faster exchange rate of amide protons with water, including residues 26-28. This impaired our ability to assess binding in semi-quantitative way, however evidence of binding of the 18-27 segment is present. pH does not seem to impact binding affinity, and higher temperature seems to weaken the affinity but a small percentage.

Statistics and reproducibility

For the rescue experiment, the m^{7}G level and protein expression level of all samples was checked by northwestern blot and western blot, respectively. Blots are representative of two biological independent experiments. For the analysis of protein complex using SDS-PAGE and native PAGE, at least two times each experiment was repeated independently with similar results.

Extended Data

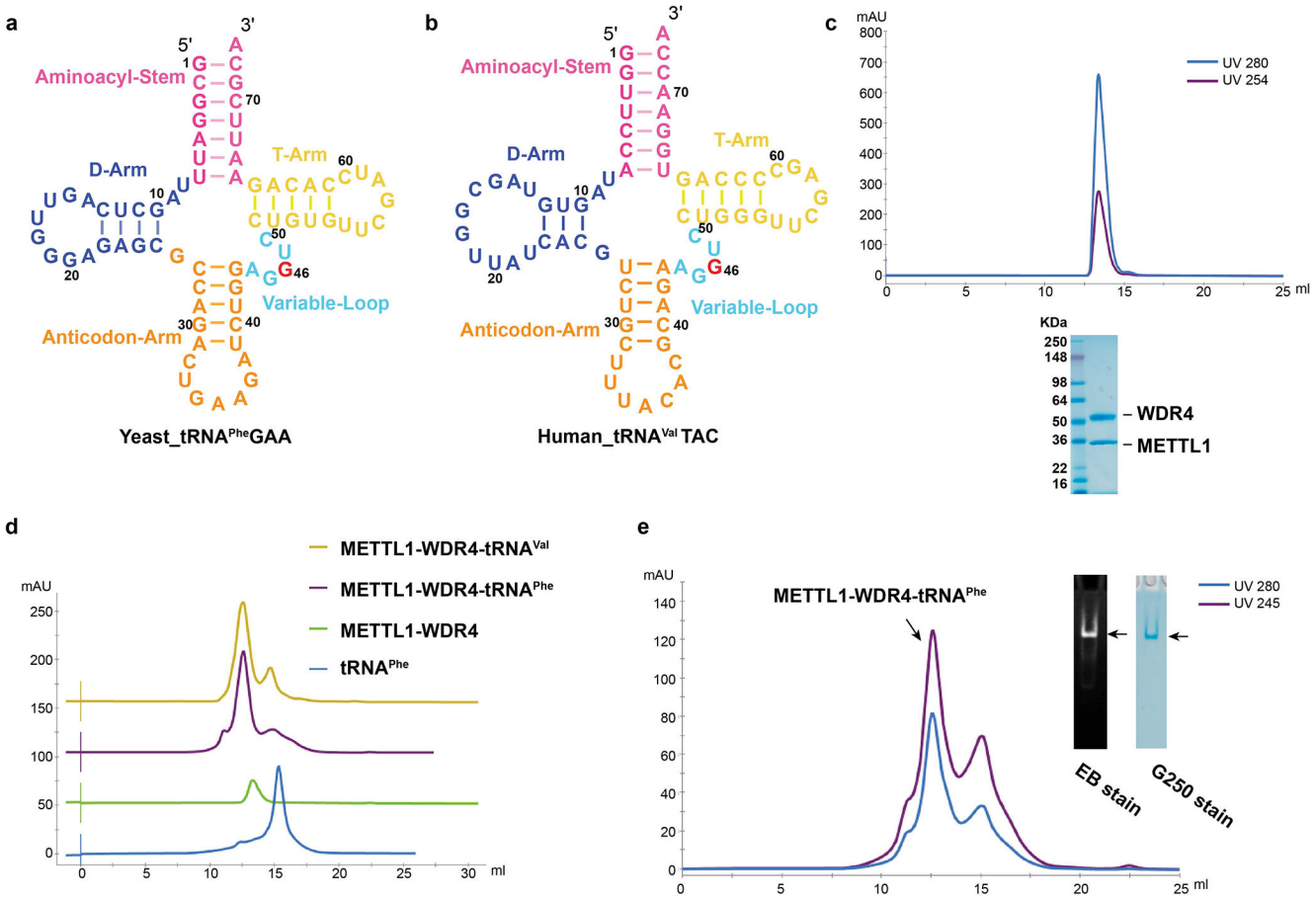

Extended Data Fig. 1 |. Sample preparation and quality check.

(**a-b**) tRNA candidates for ternary complex reconstitution. Schematic representations of yeast $tRNA^{Phe}$ and human $tRNA^{Val}$. Yeast $tRNA^{Phe}$ is a matured $tRNA^{Phe}$ purified from yeast (Sigma) (**a**). Human $tRNA^{Val}$ is an annealed single strand RNA oligos synthesized based on human $tRNA^{Val}$-TAC sequence (Horizon) (**b**). (**c**) Chromatography traces and SDS-PAGE analysis of purified METTL1-WDR4 complex (absorption at 280nm and 254nm). For gel source data, see Supplementary Fig. 3. (**d**) Gel filtration profiles of free $tRNA^{Phe}$ (blue), METTL1-WDR4 binary complex (green), METTL1-WDR4-$tRNA^{Phe}$ ternary complex (purple) and METTL1-WDR4-$tRNA^{Val}$ ternary complex (yellow) (absorption at 280nm are shown). (**e**) Identification of the reconstituted METTL1-WDR4-$tRNA^{Phe}$ ternary complex. Sample in the main peak of the reconstitution chromatography trace is analyzed by native PAGE. tRNA and protein are virtualized by EB and G250 staining separately. For gel source data, see Supplementary Fig. 4.

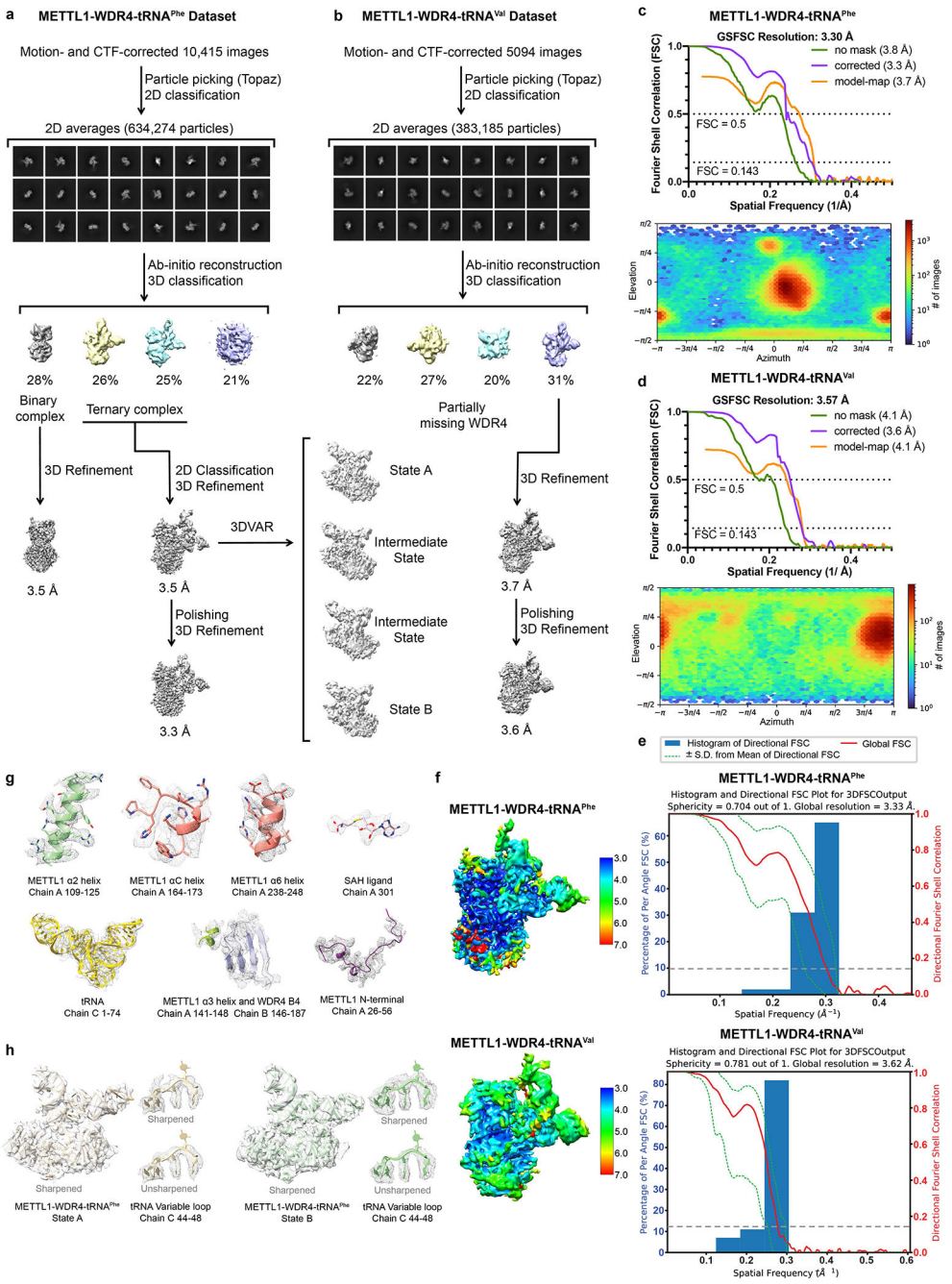

Extended Data Fig. 2 |. Cryo-EM workflows and the quality of reconstructed cryo-EM maps. (**a-b**) Workflow of 3D reconstruction of METTL1-WDR4-tRNA^{Phe} dataset (**a**) and the METTL1-WDR4-tRNA^{Val} dataset (**b**). (**c-d**) Fourier shell correlation (FSC) curves (upper panel) and orientation distributions (lower panel) of 3D reconstructed METTL1-WDR4-tRNA^{Phe}and METTL1-WDR4-tRNA^{Val} cryo-EM maps. See also Extended Data Table 1. (**e**) Histogram of directional FSC curves of METTL1-WDR4-tRNA^{Phe} dataset (upper panel) and the METTL1-WDR4-tRNA^{Val} dataset (lower panel). (**f**) Local resolutions of METTL1-WDR4-tRNA^{Phe} (upper panel) and METTL1-WDR4-tRNA^{Val} (lower panel) cryo-EM maps.

(**g**) Representative segments of sharpened cryo-EM map fitted with the model. (**h**) State A and State B models of METTL1-WDR4-tRNA^{Phe} fit in sharpened cryo-EM maps. The variable loop of tRNA fitted with sharpened (top) and unsharpened (bottom) maps from 3D variability analysis are shown in parallel with the whole model.

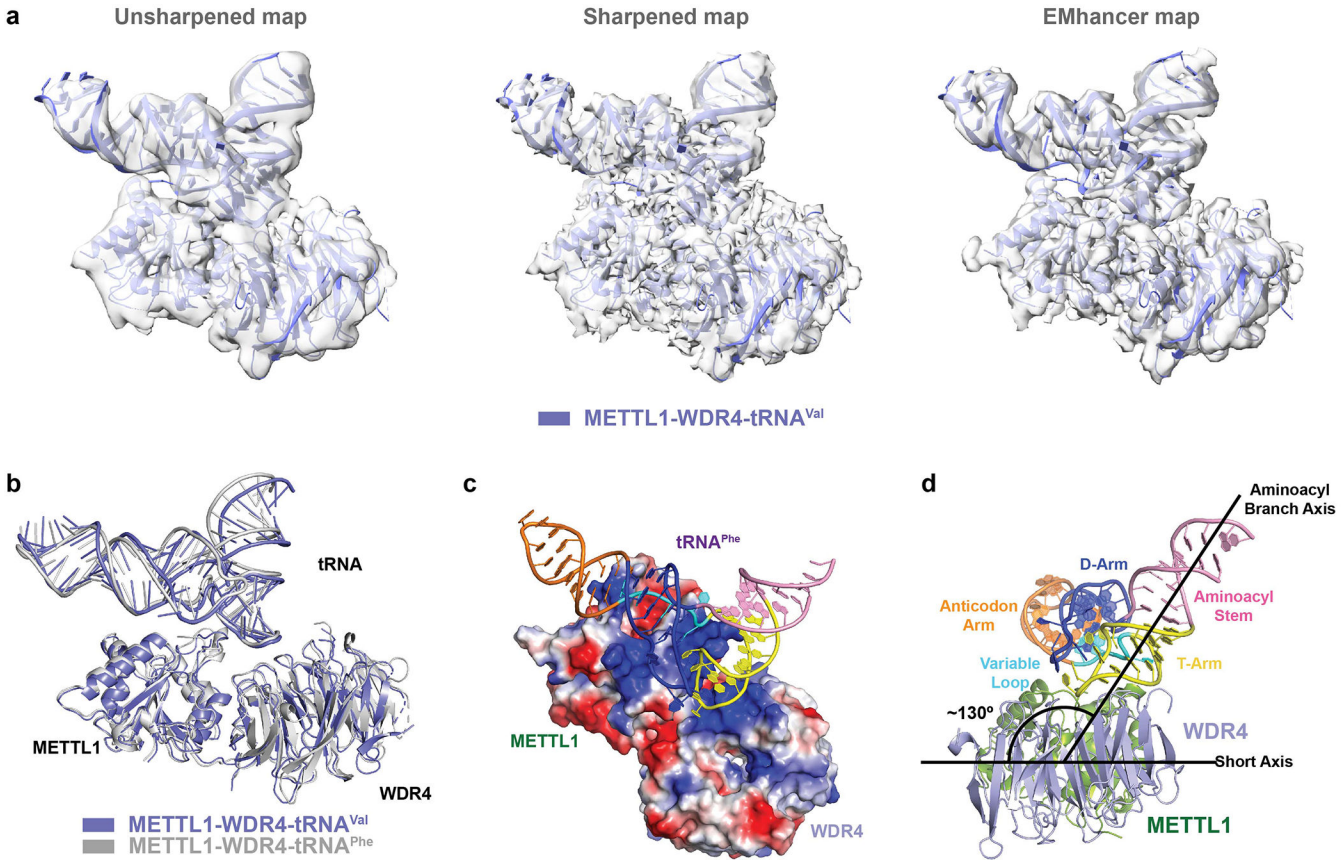

Extended Data Fig. 3 |. Similar binding mode of METTL1-WDR4 to tRNA^{Phe} and tRNA^{Val}. (**a**) Cryo-EM density maps of METTL1-WDR4-tRNA^{Val} complex and the corresponding atomic model. The unsharpened (left), sharpened (middle) and DeepEMhancer processed (right) density maps are shown. (**b**) Overall structural superposition of METTL1-WDR4-tRNA^{Val} (slate) and METTL1-WDR4-tRNA^{Phe} (white). (**c**) Electrostatic potential of METTL1 and WDR4 in ternary complex (tRNA^{Phe}). Red, negative; blue, positive. Figure was generated using PyMOL. tRNA domains are colored according to Extended Data Fig. 1a. (**d**) Tilted loading of tRNA^{Phe} onto the METTL1-WDR4 complex. Overall structure of METTL1-WDR4-tRNA^{Phe} complex from the WDR4 side. The angle between the short axis of METTL1-WDR4 and the aminoacyl-branch axis of tRNA is about 130 degrees. The angle is measured utilizing residue 213 (WDR4), residue 163 (WDR4) and base 73 of tRNA using PyMOL.

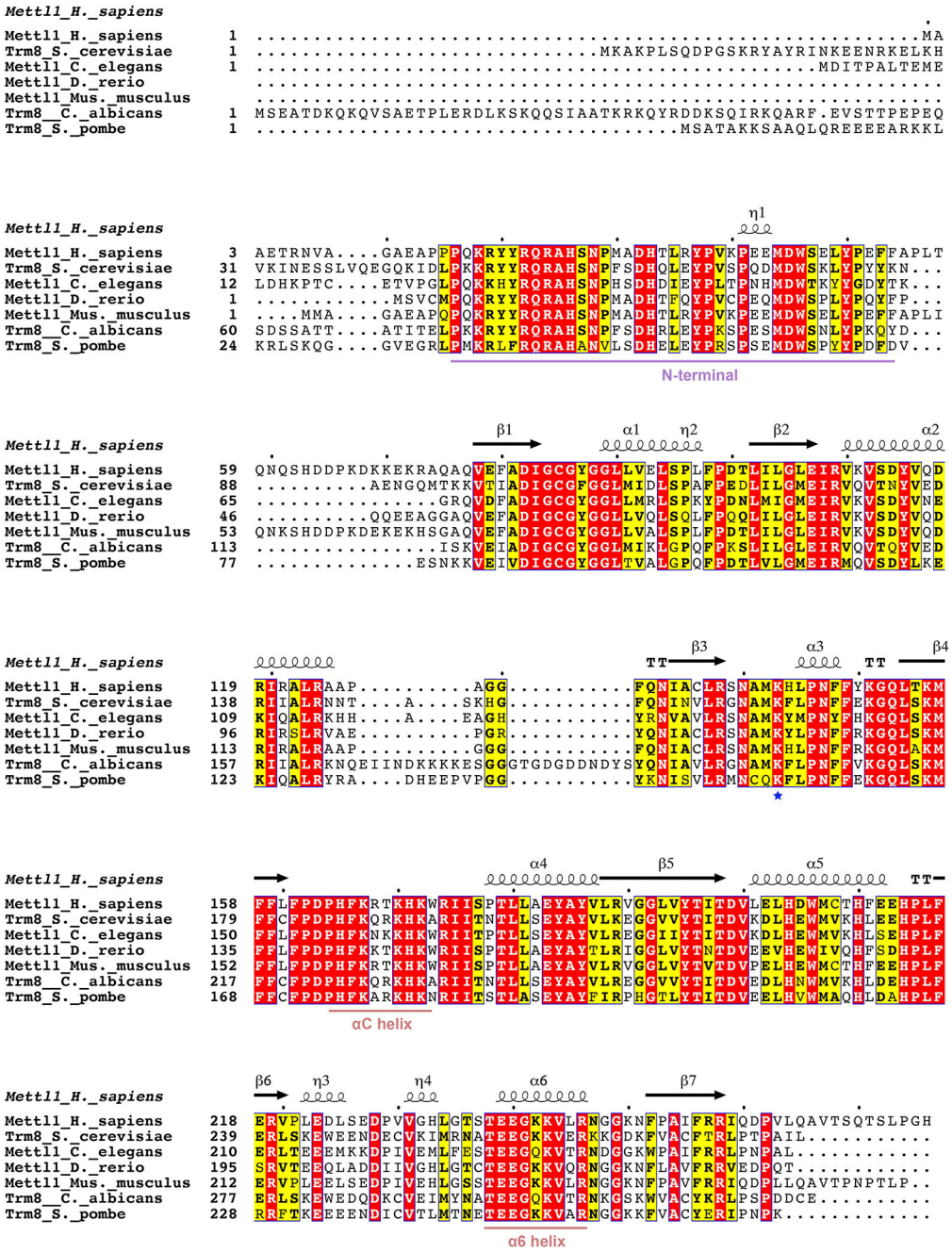

Extended Data Fig. 4 |. Sequence alignment of METTL1 proteins.

The human METTL1 protein sequence was aligned with its respective homologs. The secondary structure diagram for human METTL1 is shown on the top. Conserved residues are shaded in yellow, whereas essentially invariant residues are shown in red. The conserved N-terminal region, aC and a6 helix are underlined. K143 (key residue that interacts with WDR4) is highlighted with a blue star on the bottom. The alignment is performed with the Clustal Omega multiple sequence alignment program (EMBL-EBI) and visualized by ESPript 3.0 server.

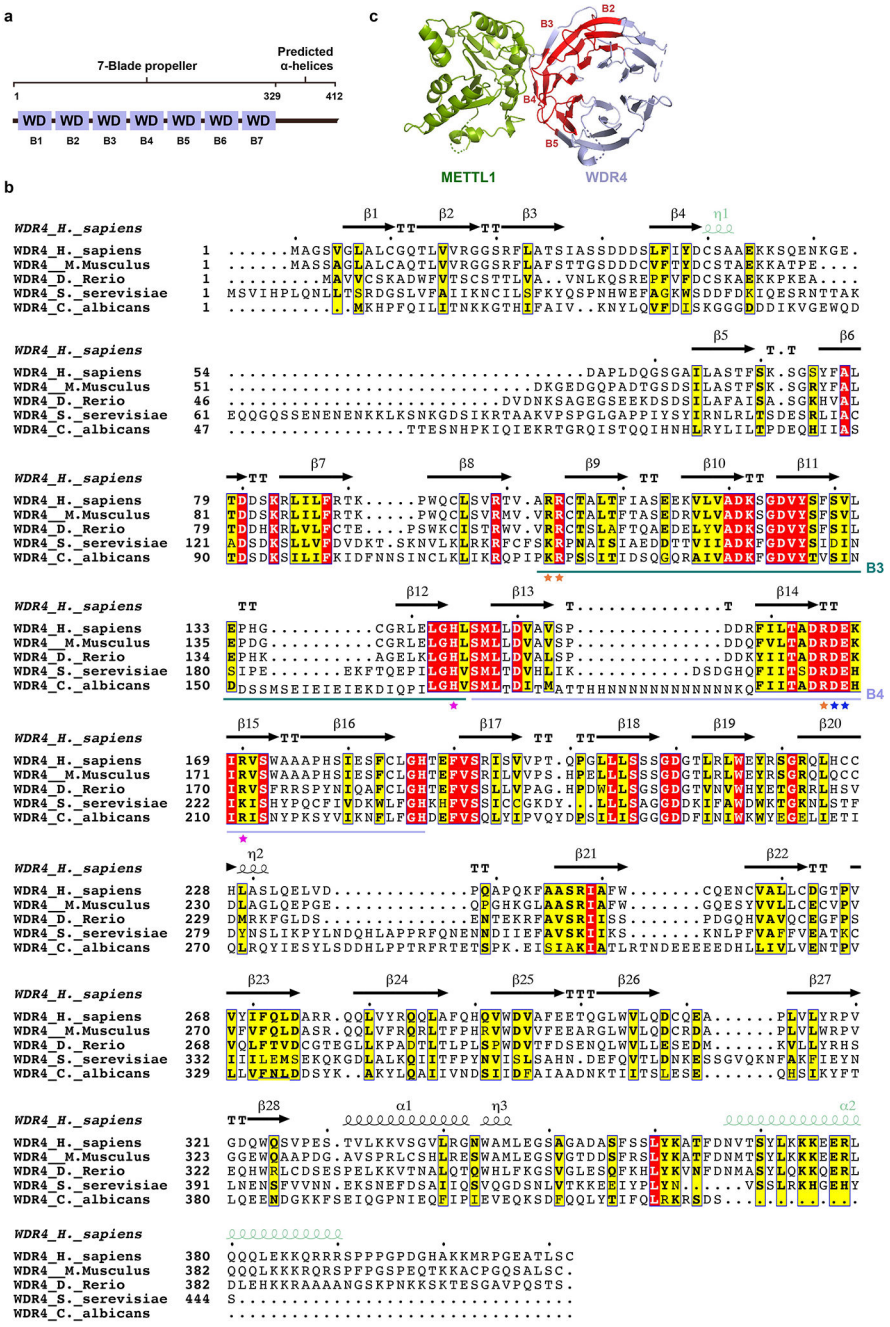

Extended Data Fig. 5. Domain organization and sequence alignment of WDR4 proteins.

(**a**) Schematic representation of full-length WDR4 domains based on sequence, secondary structure prediction and experimental structures. WD, WD family repeat domain and are numbered with B1-B7. (**b**) Sequence alignment of WDR4 proteins. The secondary structure diagram (black, based on experimental structure; pale green, based on AlphaFold prediction) for human WDR4 is shown on the top. Conserved residues are shaded in yellow, whereas essentially invariant residues are shown in red. B3 and B4 are underlined in green and blue, respectively. Key residues are highlighted with stars on the bottom. Orange stars,

residues involved in tRNA (T-arm) binding; magenta stars, patient related mutagenesis sites; blue stars, METTL1 interaction sites. The alignment is performed with the Clustal Omega multiple sequence alignment program (EMBL-EBI) and visualized by ESPript 3.0 server. (**c**) Structure of METTL1-WDR4-tRNA^{Phe} ternary complex with top view (only METTL1 and WDR4 are shown). The conserved region of B2-B5 (WDR4) is highlighted in red.

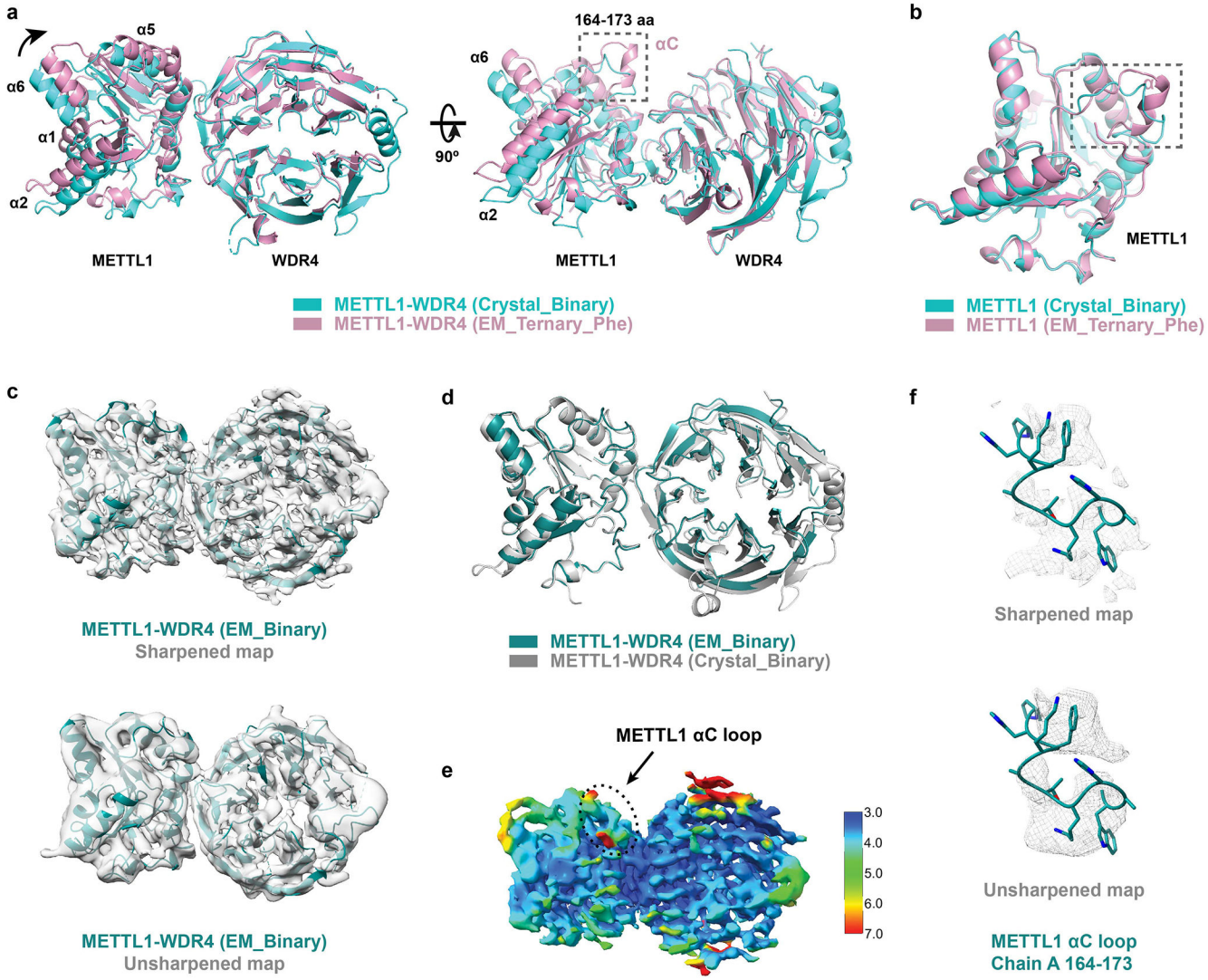

Extended Data Fig. 6 |. The conformational change of METTL1-WDR4 upon tRNA binding. (**a**)Structure comparison between METTL1-WDR4-tRNA^{Phe} and METTL1-WDR4. The structures are superposed on WDR4 protein. The tRNA in the ternary complex is not shown for a better view. METTL1-WDR4-tRNA^{Phe}, pink; METTL1-WDR4, Cyan. The α1, α2, α5 and α6 helices significantly shift toward WDR4 and tRNA side. Structural changes of the residues 164-173 fragment of METTL1 are highlighted with a dash line box. (**b**) Superposition of tRNA-free (cyan) and tRNA bound (pink) states of METTL1. The structures are superposed on METTL1 protein and only only METTL1 are shown. The loop (residues 164-173) connecting α1 and the core fold of METTL1 forms the αC helix upon

tRNA binding. (**c**) Binary complex model from METTL1-WDR4-tRNA^{Phe} cryo-EM dataset fit in sharpened (top) and unsharpened (bottom) cryo-EM maps. (**d**) Structure comparison between EM_Binary (teal) and crystal METTL1-WDR4 (gray). The METTL1 protein is superimposed. (**e**) Local resolution of binary complex map. The αC loop of METTL1 region is highlighted with dashed line circle. (**f**)The αC loop of METTL1 (EM_Binary) fit in sharpened (top) and unsharpened (bottom) cryo-EM maps.

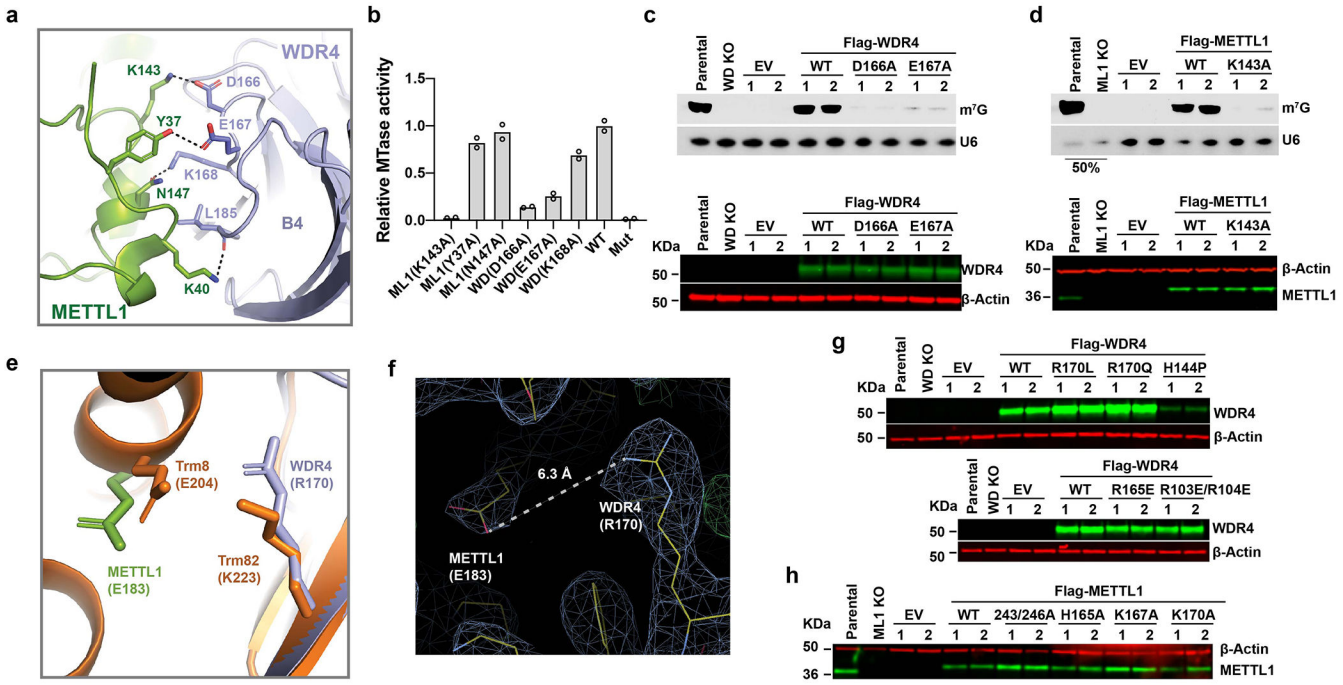

Extended Data Fig. 7 |. Essential residues of METTL1-WDR4 for MTase activity and tRNA recognition.

(**a**) Magnified view of METTL1-WDR4 interface in the crystal binary complex structure. The interactions of key residues are shown in dashed lines. K143 (METTL1) forms a salt bridge with D166 (WDR4); hydrogen bonds are formed between Y37 (METTL1) and E167 (WDR4), N147 (METTL1), and K168 (WDR4), K40 (METTL1) and mainchain of L185 (WDR4). (**b**) Relative methyltransferase activity of METTL1-WDR4 complexes expressed with indicated mutations. WT, wild type; Mut, catalytic dead double mutant (L160A/D163A). Two technical replicates were performed. (**c-d**) *In vivo* rescue experiment with METTL1 or WDR4 carrying indicated mutations in WDR4 (KO) cell lines (c) or METTL1 (KO) cell lines (d). n=2, biologically independent samples. Expression of WT and variants METTL1 or WDR4 is checked by western blot (lower panel). For gel source data, see Supplementary Fig. 5–6. (**e**) Structure comparison between METTL1-WDR4 crystal structure (PDB 7U20, METTL1, splitpea; WDR4, light blue) and Trm8-Trm82 (PDB 2VDU, orange). The WDR4 protein is superimposed. (**f**) Distance measurement between METTL1 E183 (OE2) and WDR4 R170 (NH1) in the crystal binary complex structure. 2Fo-Fc map is shown (1.2 σ). Figures were generated in Coot. (**g, h**) Western blot detection of overexpressed METTL1 or WDR4 in rescue experiments relative to Fig 2e, j. n=2, biologically independent samples. For gel source data, see Supplementary Fig. 7.

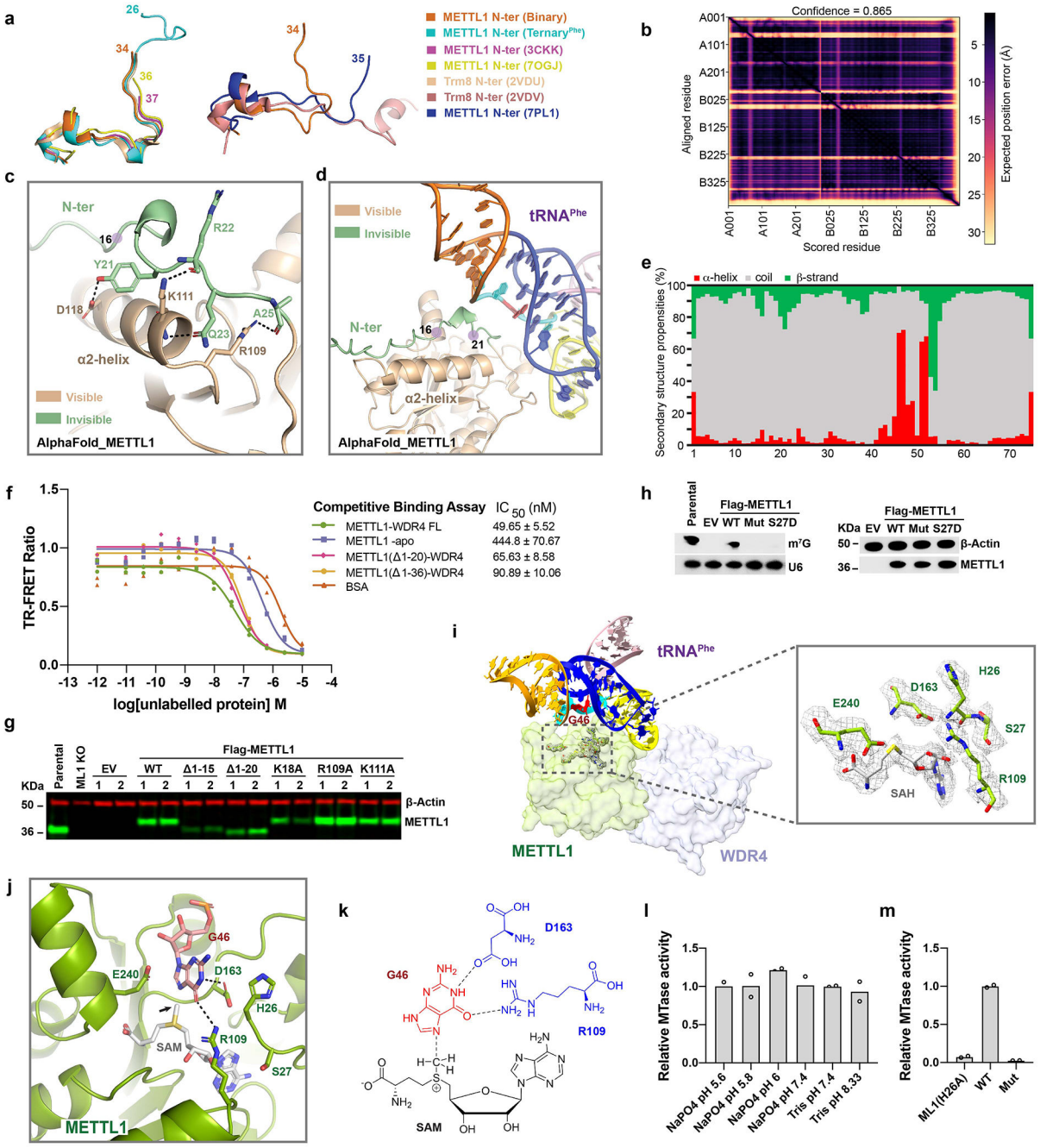

Extended Data Fig. 8 |. The METTL1 N-terminus plays important roles in catalytic regulation.

(**a**) Superimposed METTL1 N-terminus of available structures. The first visible residues of human METTL1 are labeled. (**b**) The IDDT value of the predicted METTL1-WDR4 structure. (**c**) The interactions between the N-terminal and α2 helix in AlphaFold prediction. (**d**) AlphaFold predicted METTL1 is superposed onto METTL1-WDR4-tRNA^{Phe}. The predicted residues 16-21 insert into the space between METTL1 and tRNA. (**e**) Residue-specific secondary structure propensities derived from $^{1}H_N$, ^{15}N, $^{13}C'$, $^{13}C\alpha$ and $^{13}C\beta$ chemical shifts assignments. α-helix (red), coil/unstructured (grey), β-strand (green). (**f**)

Competitive TR-FRET binding assay of labeled full-length METTL1-WDR4 with unlabeled proteins. The determined IC_{50} is listed. Two technical replicates were performed. (**g**) Western blot detection of overexpressed METTL1 or WDR4 relative to Fig. 3f. n=2, biologically independent samples. For gel source data, see Supplementary Fig. 7. (**h**) *In vivo* rescue experiment with indicated mutations in METTL1 (KO) cell lines (left). Expression of protein is checked by western blot (right). For gel source data, see Supplementary Fig. 8. (**i**) Key components of the G46 binding cavity fit in sharpened METTL1-WDR4-$tRNA^{Phe}$ cryo-EM map (mesh). Key residues and cofactor SAH are shown in stick. (**j**) Docking model of G46 flipping into the catalytic pocket with SAM bound. The transferred methyl group is indicated by arrow. Relevant elements are adjusted manually to make 180° angle and 2 Å between the guanine-N7 and S-CH_3. The potential interactions between METTL1 and the base of G46 are highlighted with dashed lines. (**k**) Schematic diagram of the docking model depicting potential interactions (dashed lines) between G46 and SAM in the METTL1 active site prior to methyl transfer. (**l-m**) Relative methyltransferase activity of METTL1-WDR4 with buffer pH ranging from 5.6 to 8.33 (l) and indicated mutation (m). Two technical replicates were performed.

Extended Data Table 1.

X-ray data collection and refinement statistics

	METTL1-WDR4 PDB ID 7U20
Data collection	
Space group	$C222_1$
Cell dimensions	
a, *b*, *c* (Å)	124.41, 194.57, 86.35
α, β, γ (°)	90.00, 90.00, 90.00
Resolution (Å)	47.87-3.09 (3.31-3.09) *
$CC_{1/2}$	0.983 (0.320)
$I / \sigma I$	5.1 (0.9)
Completeness (%)	99.0 (97.5)
Redundancy	4.6 (4.7)
Refinement	
Resolution (Å)	47.87-3.10
No. reflections	18971
R_{work} / R_{free}	0.2215/0.2708
No. atoms	
Protein	4327
Ligand/ion	15
Water	12
B-factors	
Protein	75.04
Ligand/ion	95.02
Water	55.40
R.m.s. deviations	

	METTL1-WDR4 PDB ID 7U20
Bond lengths (Å)	0.002
Bond angles (°)	0.435

	Crystal 1 name	Crystal 2 name
Data collection		
Space group		
Cell dimensions		
a, *b*, *c* (Å)		
α, β, γ (°)		
Resolution (Å)	##(high res shell) *	
R_{sym} or R_{merge}	##(high res shell)	
$I / \sigma I$	##(high res shell)	
Completeness (%)	##(high res shell)	
Redundancy	##(high res shell)	
Refinement		
Resolution (Å)		
No. reflections		
R_{work} / R_{free}		
No. atoms		
Protein		
Ligand/ion		
Water		
B-factors		
Protein		
Ligand/ion		
Water		
R.m.s deviations		
Bond lengths (Å)		
Bond angles (°)		

	Native	Crystal 1 name		Crystal 2 name		
Data collection						
Space group		common #		common #		
Cell dimensions						
a, *b*, *c* (Å)		common #		common #		
α, β, γ (°)		common #		common #		
	Peak	***Inflection***	***Remote***	***Peak***	***Inflection***	***Remote***
Wavelength	#	#	#	#	#	#
Resolution (Å)	#	#	#	#	#	#
R_{sym} or R_{merge}	#	#	#	#	#	#
$I / \sigma I$	#	#	#	#	#	#

	Native		Crystal 1 name		Crystal 2 name	
Completeness (%)	#	#	#	#	#	#
Redundancy	#	#	#	#	#	#
Refinement						
Resolution (Å)		common #			common #	
No. reflections						
R_{work} / R_{free}						
No. atoms						
Protein						
Ligand/ion						
Water						
B-factors						
Protein						
Ligand/ion						
Water						
R.m.s deviations						
Bond lengths (Å)						
Bond angles (°)						

* Values in parentheses are for highest-resolution shell.

* Number of xtals for each structure should be noted in footnote. *Values in parentheses are for highest-resolution shell.

* Number of xtals for each structure should be noted in footnote. *Values in parentheses are for highest-resolution shell.

Extended Data Table 2.

Cryo-EM data collection, refinement and validation statistics

	METTL1-WDR4-tRNA^{Phe} -SAH (EMDB-26990) (PDB 8CTH)	METTL1-WDR4-tRNA^{Val} (EMDB-26991) (PDB 8CTI)
Data collection and processing		
Magnification	81,000	81,000
Voltage (kV)	300	300
Electron exposure (e–/Å^2)	50.0	51.8
Defocus range (μm)	−1.0 to −2.0	0.8 to −2.2
Pixel size (Å)	1.08	0.825
Symmetry imposed	C1	C1
Initial particle images (no.)	634,274	383,185
Final particle images (no.)	266,099	115,797
Map resolution (Å)	3.3	3.6
FSC threshold	0.143	0.143
Refinement		
Initial model used (PDB code)	1EHZ	3JAG
Model resolution (Å)	3.2/3.7	3.5/4.1
FSC threshold	0.143/0.5	0.143/0.5
Map sharpening *B* factor (Å^2)	125.3	147.8
Model composition		

	METTL1-WDR4-tRNA^{Phe} -SAH (EMDB-26990) (PDB 8CTH)	METTL1-WDR4-tRNA^{Val} (EMDB-26991) (PDB 8CTI)
Non-hydrogen atoms	5,544	5,297
Protein residues	495	473
Nucleotide	74	71
Ligands	1	0
R.m.s. deviations		
Bond lengths (Å)	0.003	0.011
Bond angles (°)	0.541	0.793
Validation		
MolProbity score	1.80	1.76
Clashscore	11.80	11.62
Poor rotamers (%)	0.00	0.49
Ramachandran plot		
Favored (%)	96.68	96.95
Allowed (%)	3.32	3.05
Disallowed (%)	0.00	0.00

Supplementary Material

Refer to Web version on PubMed Central for supplementary material.

Acknowledgments

E.A.O. is supported by the Pew Latin American Fellows Program in the Biomedical Sciences from Pew Charitable Trusts and by a fellowship from the Damon Runyon Cancer Research Foundation (DRG-2378-19). R.I.G. is supported by an Outstanding Investigator Award (R35CA232115) from the National Cancer Institute (NCI) of the NIH. This work was in part supported by NIH grants R01 CA218278 (E.S.F.), R01 CA214608 (E.S.F.), the Mark Foundation for Cancer Research (Mark Foundation Emerging Leader Award 19-001-ELA to E.S.F.), and Cancer Research Institute (Irvington Postdoctoral Fellowship CRI 3442 to S.S.R.B.). This research was, in part, supported by the National Cancer Institute's National Cryo-EM Facility at the Frederick National Laboratory for Cancer Research under contract HSSN261200800001E. We thank the staff at the Harvard Cryo-EM Center for Structural Biology for their support during grid screening and data collection. This research used resources of the Advanced Photon Source, a US Department of Energy (DOE) Office of Science User Facility operated for the DOE Office of Science by Argonne National Laboratory under contract number SE-AC02-06CH11357. We acknowledge the SBGrid consortium for assistance with high-performance computing.

Data availability statement

The CryoEM structures of METTL1-WDR4-tRNA (Phe) and METTL1-WDR4-tRNA (Val), and X-ray crystal structure of METTL1-WDR4 have been deposited to the Protein Data Bank (PDB) under accession number 8CTH, 8CTI and 7U20, respectively. The cryo-EM density maps of METTL1-WDR4-tRNA (Phe) and METTL1-WDR4-tRNA (Val) have been deposited in the Electron Microscopy Data Bank (EMDB) under accession numbers 26990 and 26991. Several structural coordinates in the PDB database were used in this study, which can be located by accession numbers 1EHZ, 2VDU, 3JAG, 3CKK, 7OGJ, 2VDV and 7PL1. NMR resonance assignments were deposited to the BMRB under accession number 51362.

References

1. Roundtree IA, Evans ME, Pan T & He C Dynamic RNA Modifications in Gene Expression Regulation. Cell 169, 1187–1200, doi:10.1016/j.cell.2017.05.045 (2017). [PubMed: 28622506]
2. Frye M, Harada BT, Behm M & He C RNA modifications modulate gene expression during development. Science 361, 1346–1349, doi:10.1126/science.aau1646 (2018). [PubMed: 30262497]
3. Barbieri I & Kouzarides T Role of RNA modifications in cancer. Nat Rev Cancer, doi:10.1038/s41568-020-0253-2 (2020).
4. Motorin Y & Helm M tRNA stabilization by modified nucleotides. Biochemistry 49, 4934–4944 (2010). [PubMed: 20459084]
5. Tomikawa C 7-Methylguanosine Modifications in Transfer RNA (tRNA). Int J Mol Sci 19, doi:10.3390/ijms19124080 (2018).
6. Alexandrov A et al. Rapid tRNA decay can result from lack of nonessential modifications. Molecular cell 21, 87–96 (2006). [PubMed: 16387656]
7. Whipple JM, Lane EA, Chernyakov I, D'Silva S & Phizicky EM The yeast rapid tRNA decay pathway primarily monitors the structural integrity of the acceptor and T-stems of mature tRNA. Genes Dev 25, 1173–1184, doi:10.1101/gad.2050711.10.1101/gad.2050711 (2011). [PubMed: 21632824]
8. Alexandrov A, Martzen MR & Phizicky EM Two proteins that form a complex are required for 7-methylguanosine modification of yeast tRNA. Rna 8, 1253–1266 (2002). [PubMed: 12403464]
9. Leulliot N et al. Structure of the yeast tRNA m7G methylation complex. Structure 16, 52–61, doi:10.1016/j.str.2007.10.025 (2008). [PubMed: 18184583]
10. Orellana EA et al. METTL1-mediated m(7)G modification of Arg-TCT tRNA drives oncogenic transformation. Mol Cell, doi:10.1016/j.molcel.2021.06.031 (2021).
11. Dai Z et al. N(7)-Methylguanosine tRNA modification enhances oncogenic mRNA translation and promotes intrahepatic cholangiocarcinoma progression. Mol Cell, doi:10.1016/j.molcel.2021.07.003 (2021).
12. Ma J et al. METTL1/WDR4-mediated m7G tRNA modifications and m7G codon usage promote mRNA translation and lung cancer progression. Molecular Therapy 29, 3422–3435 (2021). [PubMed: 34371184]
13. Han H et al. N7-methylguanosine tRNA modification promotes esophageal squamous cell carcinoma tumorigenesis via the RPTOR/ULK1/autophagy axis. Nature communications 13, 1–15 (2022).
14. Chen J et al. Aberrant translation regulated by METTL1/WDR4-mediated tRNA N7-methylguanosine modification drives head and neck squamous cell carcinoma progression. Cancer Communications 42, 223–244 (2022). [PubMed: 35179319]
15. Shaheen R et al. Mutation in WDR4 impairs tRNA m(7)G46 methylation and causes a distinct form of microcephalic primordial dwarfism. Genome Biol 16, 210, doi:10.1186/s13059-015-0779-x (2015). [PubMed: 26416026]
16. Braun DA et al. Mutations in WDR4 as a new cause of Galloway-Mowat syndrome. Am J Med Genet A 176, 2460–2465, doi:10.1002/ajmg.a.40489 (2018). [PubMed: 30079490]
17. Trimouille A et al. Further delineation of the phenotype caused by biallelic variants in the WDR4 gene. Clin Genet 93, 374–377, doi:10.1111/cge.13074 (2018). [PubMed: 28617965]
18. Cartlidge RA et al. The tRNA methylase METTL1 is phosphorylated and inactivated by PKB and RSK in vitro and in cells. The EMBO journal 24, 1696–1705 (2005). [PubMed: 15861136]
19. Torres AG, Batlle E & de Pouplana LR Role of tRNA modifications in human diseases. Trends in molecular medicine 20, 306–314 (2014). [PubMed: 24581449]
20. Suzuki T The expanding world of tRNA modifications and their disease relevance. Nat Rev Mol Cell Biol 22, 375–392, doi:10.1038/s41580-021-00342-0 (2021). [PubMed: 33658722]
21. Pan T Modifications and functional genomics of human transfer RNA. Cell Res 28, 395–404, doi:10.1038/s41422-018-0013-y (2018). [PubMed: 29463900]

22. Schimmel P The emerging complexity of the tRNA world: mammalian tRNAs beyond protein synthesis. Nat Rev Mol Cell Biol 19, 45–58, doi:10.1038/nrm.2017.77 (2018). [PubMed: 28875994]
23. Lin S et al. Mettl1/Wdr4-Mediated m(7)G tRNA Methylome Is Required for Normal mRNA Translation and Embryonic Stem Cell Self-Renewal and Differentiation. Mol Cell 71, 244–255 e245, doi:10.1016/j.molcel.2018.06.001 (2018). [PubMed: 29983320]
24. Matsumoto K et al. RNA recognition mechanism of eukaryote tRNA (m7G46) methyltransferase (Trm8-Trm82 complex). FEBS Lett 581, 1599–1604, doi:10.1016/j.febslet.2007.03.023 (2007). [PubMed: 17382321]
25. Jumper J et al. Highly accurate protein structure prediction with AlphaFold. Nature 596, 583–589 (2021). [PubMed: 34265844]
26. Shi H & Moore PB The crystal structure of yeast phenylalanine tRNA at 1.93 Å resolution: a classic structure revisited. Rna 6, 1091–1105 (2000). [PubMed: 10943889]
27. Blersch KF et al. Structural model of the M7G46 Methyltransferase TrmB in complex with tRNA. RNA Biol, 1–14, doi:10.1080/15476286.2021.1925477 (2021).
28. Punjani A, Rubinstein JL, Fleet DJ & Brubaker MA cryoSPARC: algorithms for rapid unsupervised cryo-EM structure determination. Nature methods 14, 290–296 (2017). [PubMed: 28165473]
29. Yue H et al. Rapid “mix and read” assay for scalable detection of SARS-CoV-2 antibodies in patient plasma. (2020).
30. Kabsch W Xds. Acta Crystallographica Section D: Biological Crystallography 66, 125–132 (2010). [PubMed: 20124692]
31. Liebschner D et al. Macromolecular structure determination using X-rays, neutrons and electrons: recent developments in Phenix. Acta Crystallographica Section D: Structural Biology 75, 861–877 (2019). [PubMed: 31588918]
32. Chen VB et al. MolProbity: all-atom structure validation for macromolecular crystallography. Acta Crystallographica Section D: Biological Crystallography 66, 12–21 (2010). [PubMed: 20057044]
33. Morin A et al. Cutting edge: Collaboration gets the most out of software. elife 2, e01456 (2013). [PubMed: 24040512]
34. Zheng SQ et al. MotionCor2: anisotropic correction of beam-induced motion for improved cryo-electron microscopy. Nature methods 14, 331–332 (2017). [PubMed: 28250466]
35. Bepler T et al. Positive-unlabeled convolutional neural networks for particle picking in cryo-electron micrographs. Nature methods 16, 1153–1160 (2019). [PubMed: 31591578]
36. Zivanov J, Nakane T & Scheres SH A Bayesian approach to beam-induced motion correction in cryo-EM single-particle analysis. IUCrJ 6, 5–17 (2019).
37. Punjani A, Zhang H & Fleet DJ Non-uniform refinement: adaptive regularization improves single-particle cryo-EM reconstruction. Nature methods 17, 1214–1221 (2020). [PubMed: 33257830]
38. Punjani A & Fleet DJ 3D variability analysis: Resolving continuous flexibility and discrete heterogeneity from single particle cryo-EM. Journal of Structural Biology 213, 107702 (2021). [PubMed: 33582281]
39. Aiyer S, Zhang C, Baldwin PR & Lyumkis D in CryoEM 161-187 (Springer, 2021).
40. Sanchez-Garcia R et al. DeepEMhancer: a deep learning solution for cryo-EM volume post-processing. Communications biology 4, 1–8 (2021). [PubMed: 33398033]
41. Pettersen EF et al. UCSF ChimeraX: Structure visualization for researchers, educators, and developers. Protein Science 30, 70–82 (2021). [PubMed: 32881101]
42. Emsley P, Lohkamp B, Scott WG & Cowtan K Features and development of Coot. Acta Crystallogr D Biol Crystallogr 66, 486–501, doi:10.1107/S0907444910007493 (2010). [PubMed: 20383002]
43. Delaglio F et al. NMRPipe: a multidimensional spectral processing system based on UNIX pipes. Journal of biomolecular NMR 6, 277–293 (1995). [PubMed: 8520220]
44. Vranken WF et al. The CCPN data model for NMR spectroscopy: development of a software pipeline. Proteins: structure, function, and bioinformatics 59, 687–696 (2005).

45. Hyberts SG, Takeuchi K & Wagner G Poisson-gap sampling and forward maximum entropy reconstruction for enhancing the resolution and sensitivity of protein NMR data. Journal of the American Chemical Society 132, 2145–2147 (2010). [PubMed: 20121194]

46. Hyberts SG, Milbradt AG, Wagner AB, Arthanari H & Wagner G Application of iterative soft thresholding for fast reconstruction of NMR data non-uniformly sampled with multidimensional Poisson Gap scheduling. Journal of biomolecular NMR 52, 315–327 (2012). [PubMed: 22331404]

47. Shen Y & Bax A Protein backbone and sidechain torsion angles predicted from NMR chemical shifts using artificial neural networks. Journal of biomolecular NMR 56, 227–241 (2013). [PubMed: 23728592]

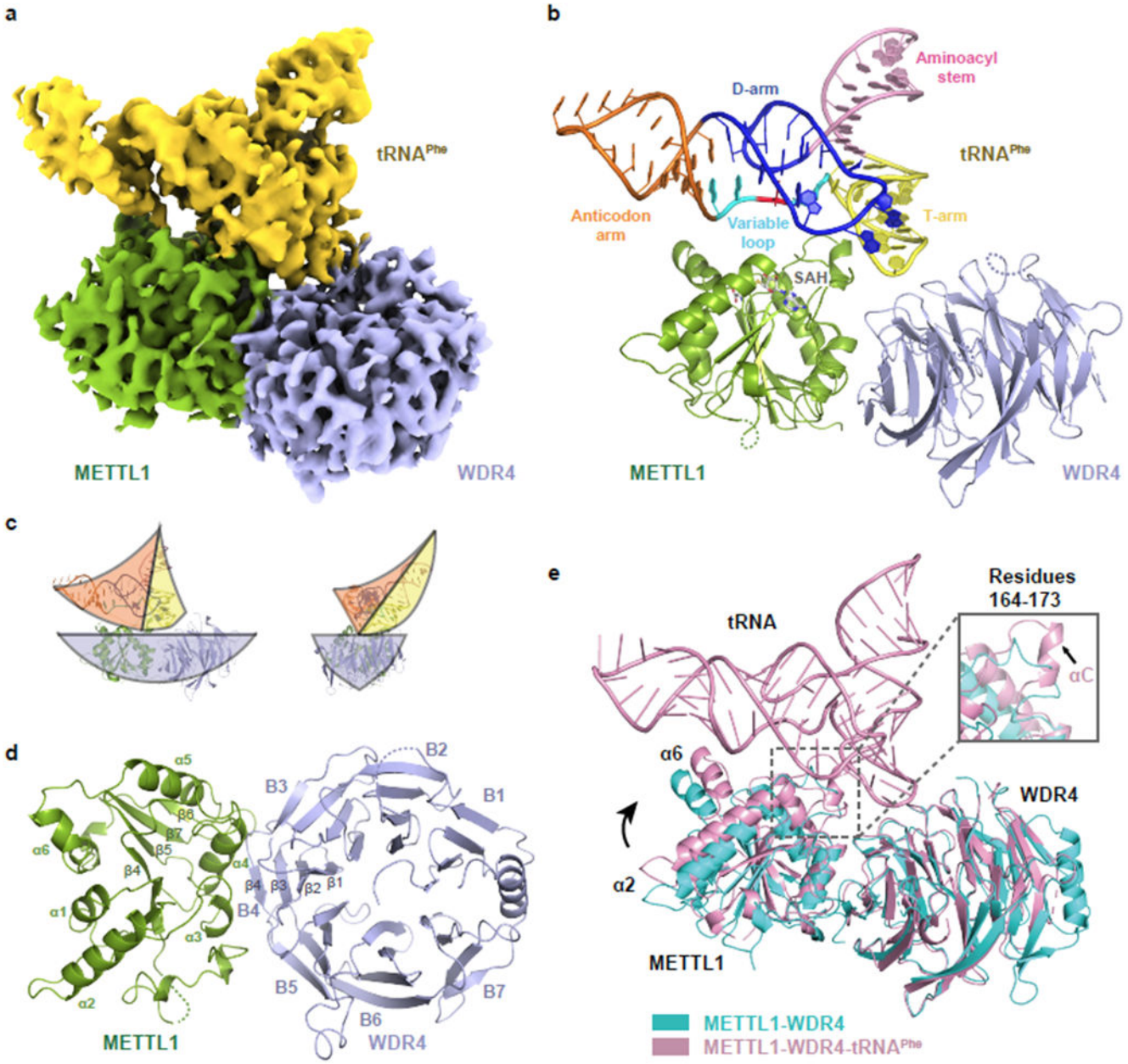

Fig. 1 |. METTL1-WDR4 provides a platform for specific tRNA loading

(**a-b**) Cryo-EM density map of METTL1-WDR4-tRNA^{Phe} complex and corresponding atomic model. The sharpened map is shown. METTL1, splitpea; WDR4, light blue; tRNA^{Phe}, yellow; tRNA domains are colored according to Extended Data Fig. 1a. The G46 is highlighted in red. (**c**) Sail boat model of METTL1-WDR4-tRNA^{Phe} ternary complex in side view (left) and front view (right). (**d**) X-ray crystal structure of full-length METTL1-WDR4 binary complex. METTL1 (splitpea) and WDR4 (light blue) are shown in cartoon representation. Secondary structure elements are numbered. (**e**) Structural comparison between METTL1-WDR4-tRNA^{Phe} complex (pink) and METTL1-WDR4 binary complex

(cyan). The two structures are superimposed on WDR4 proteins. Magnified view of METTL1 (residues 164-173) shows the αC helix that is formed upon tRNA binding.

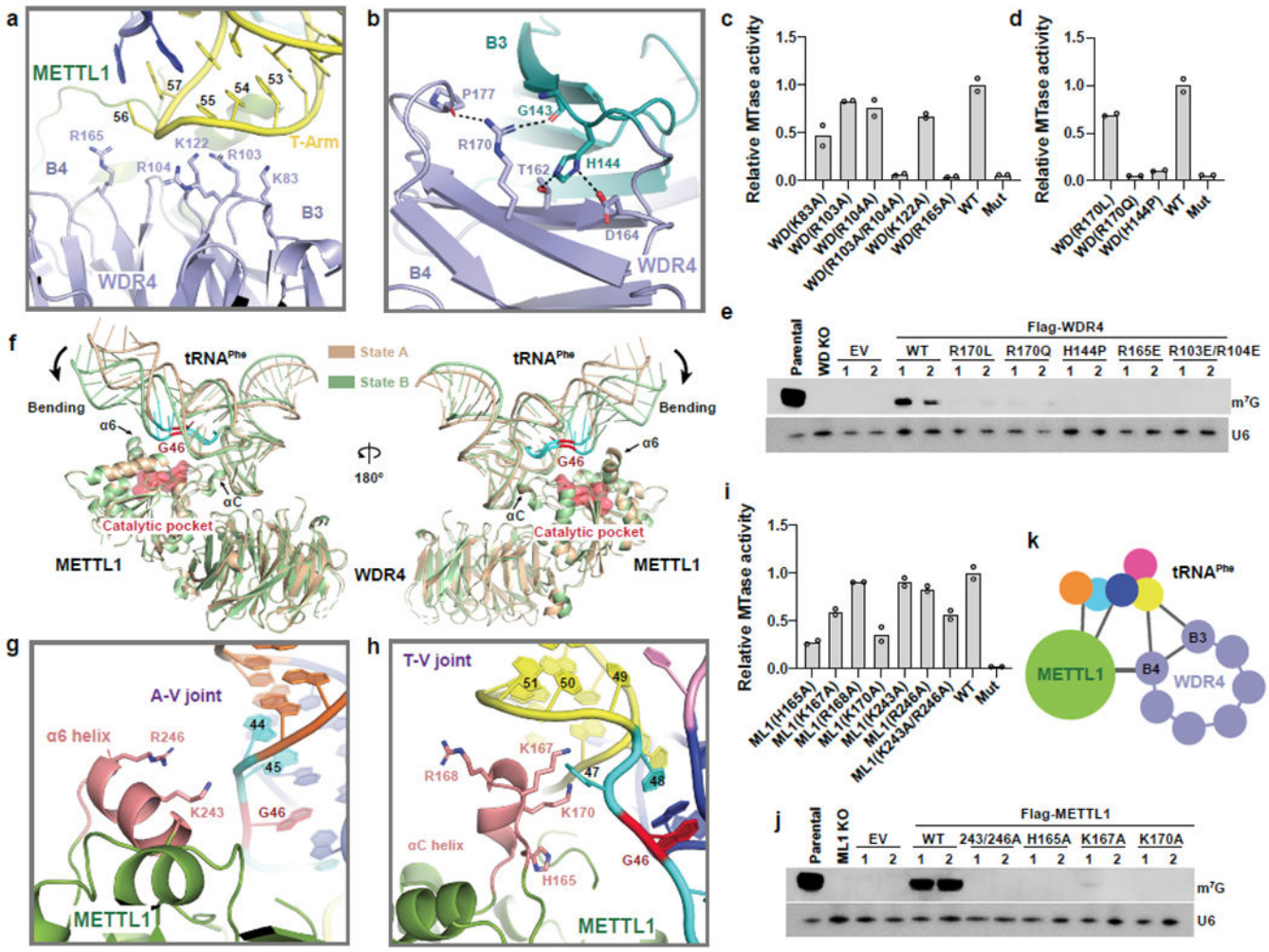

Fig. 2 |. tRNA recognition by METTL1 and WDR4

(**a**) WDR4 binds the T-arm of $tRNA^{Phe}$. Positively charged residues on B3 and B4 are modeled based on crystal structure. (**b**) Interactions between WDR4 B3 (dark teal) and B4 (light blue) in the crystal structure of METTL1-WDR4. The interactions of disease-related sites, R170 and H144, are highlighted. (**c-d**) Relative methyltransferase activity of indicated mutations in (a) and (b). WT, wild type; Mut, catalytic dead mutant (L160A/D163A). Two technical replicates were performed. (**e**) *In vivo* rescue experiment with WDR4 carrying the patient-derived mutations and tRNA-binding sites mutations. WD KO, WDR4 knockout; EV, empty vector. n=2, biologically independent samples. For protein expression, see Extended Data Fig. 7e. For gel source data, see Supplementary Fig. 1. (**f**) Superposition of different states (state A, wheat; state B, pale green) of METTL1-WDR4-$tRNA^{Phe}$ complex in two views. The two structures are superposed on METTL1 proteins. G46 and catalytic pocket are highlighted in red; tRNA variable loop, cyan. (**g-h**) Helices αC and α6 of METTL1 recognize tRNA. Magnified view of αC helix interacts with T-V joint (g) and α6 helix with A-V joint (h). Variable loop, cyan; helices αC and α6, salmon; T-V joint and A-V joint, joint region of variable loop with T-arm and anticodon-arm, respectively. Positively charged residues on helices αC and α6 are modeled based on crystal

structure. (**i**) Relative methyltransferase activity of METTL1-WDR4 complexes expressed with indicated mutations. Two technical replicates were performed. (**j**) *In vivo* rescue experiment with METTL1 variants relative to (i). n=2, biologically independent samples. For protein expression, see Extended Data Fig. 7f. For gel source data, see Supplementary Fig. 1. (**k**) Scaffold model of METTL1 (green), $tRNA^{Phe}$ (color coded relative to Fig. 1b), WDR4 (light blue, B3 and B4 are labeled).

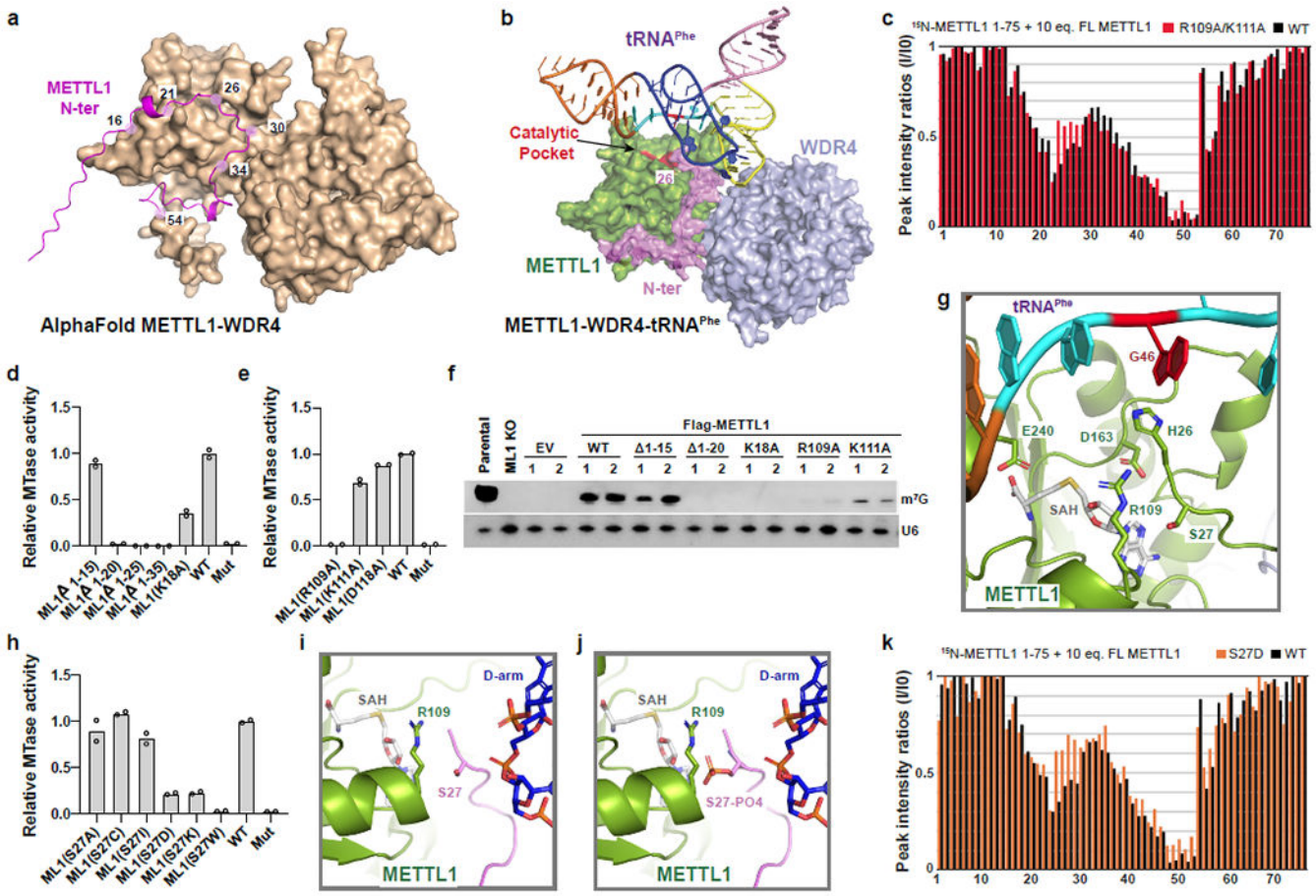

Fig. 3 |. The essential roles of METTL1 N-terminus.

(**a**) The AlphaFold prediction of METTL1-WDR4. The METTL1 N-terminal (residues 1-54) is in cartoon representation (magenta) and annotated residues are highlighted. Residues 366-412 of WDR4 are hidden for better view. The IDDT is shown in Extended Data Fig. 8b. (**b**) The METTL1 N-terminus (magenta) inserts into the catalytic pocket (red) in METTL1-WDR4-tRNA^{Phe} cryo-EM structure. Proteins are shown in surface representation. Location of residue 26 is highlighted. (**c**) NMR peak intensity ratios plotted against METTL1 1-75 sequence. Ratios are calculated as I/I_0 corresponding to the ^{15}N-^{1}H-HSQC spectra of METTL1 1-75 in the presence of 10 molar equivalent of full-length WT METTL1 (black) or R109A/K111A METTL1 (red) divided by those of METTL1 1-75. (**d-e**) Relative methyltransferase activity of METTL1-WDR4 complexes expressed with indicated truncations or mutations. Two technical replicates were performed. (**f**) *In vivo* rescue experiment with METTL1 variants. n=2, biologically independent samples. For protein expression, see Extended Data Fig. 8g. For gel source data, see Supplementary Fig. 2. (**g**) The catalytic pocket of METTL1 in METTL1-WDR4-tRNA^{Phe}. Relative residues are shown in stick representations. G46 is highlighted in red. (**h**) Relative methyltransferase activity of METTL1-WDR4 complexes expressed with indicated METTL1 mutants. Two technical replicates were performed. (**i,j**) Steric hindrance model of S27 phosphorylation. Sidechains are modeled based on AlphaFold prediction. The sidechain of S27 points to R109 (**i**). Substitution of S27 for its phosphorylated analog leads to a steric clash with R109 (**j**).

(**k**) NMR peak intensity ratios plotted against METTL1 1-75 sequence. Ratios are calculated as I/I_0 corresponding to the ^{15}N-^{1}H-HSQC spectra of WT METTL1 1-75 (black) or S27D METTL1 1-75 (orange) in the presence of 10 molar equivalent of full-length WT METTL1 divided by those of the corresponding METTL1 1-75.

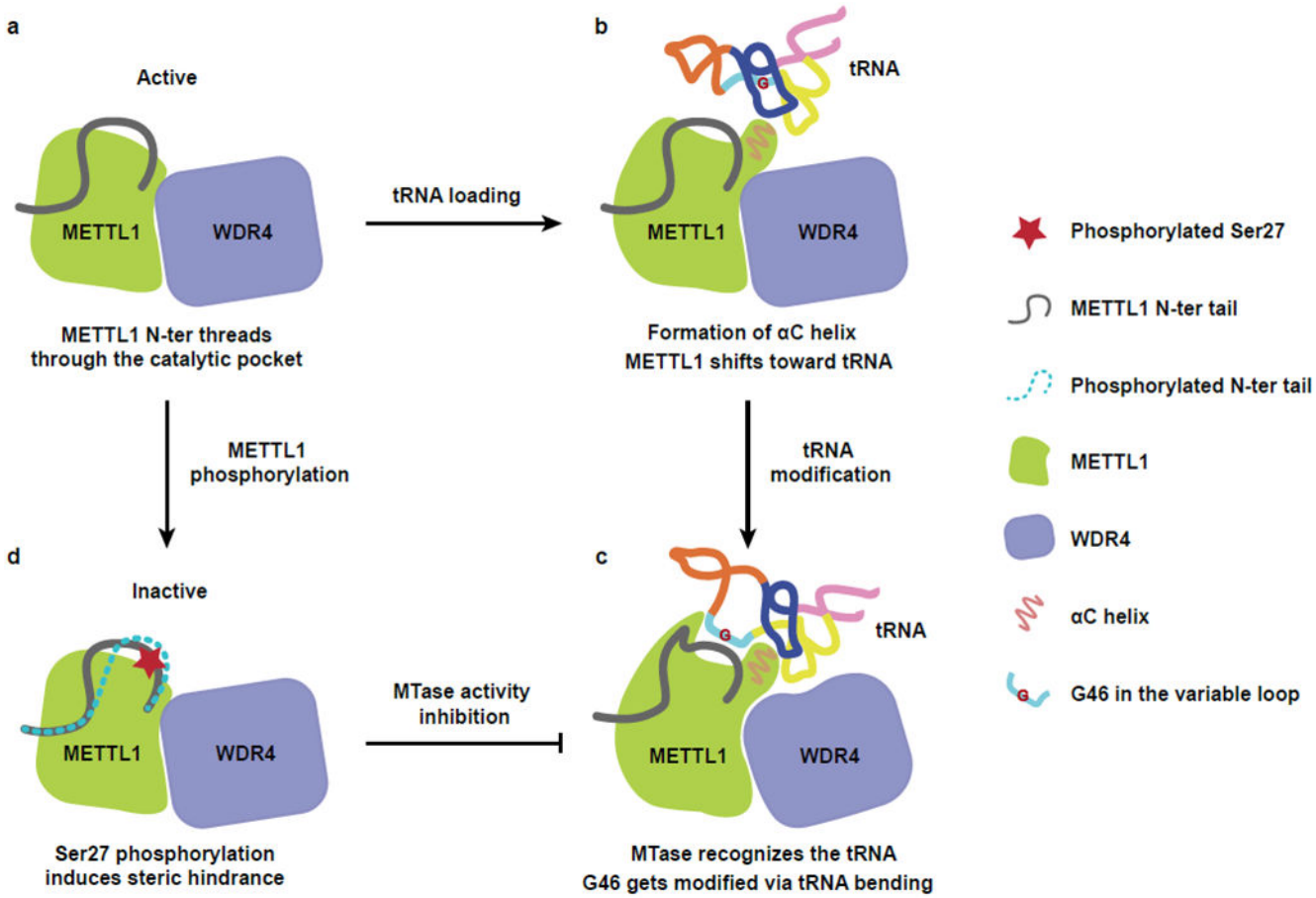

Fig. 4 |. Model of human METTL1-WDR4 in substrate recognition, modification and catalytic regulation.

(**a**) The cartoon representation of METTL1-WDR4 complex with the U-shaped METTL1 N-terminus that contributes to the catalytic pocket. (**b**) The tRNA loads to METTL1-WDR4 platform with specific binding mode. Upon the tRNA binding, residues 164-173 of METTL1 form the αC helix, and METTL1 shifts toward the tRNA. (**c**) The METTL1-WDR4 recognizes tRNA with essential features including the N-terminal tail, helices αC and α6 of METTL1 and B3-B4 of WDR4. The tRNA undergoes bending to facilitate G46 flipping into the catalytic pocket to be modified. (**d**) The N-terminal region (residues 24-27) of METTL shift away when S27 is phosphorylated. Phosphorylated S27 and N-terminus are highlighted with red star and blue dashed lines, respectively.